Click Here for Full Article

Structure and dynamics of the Columbia River tidal plume front

Levi F. Kilcher[1] and Jonathan D. Nash[1]

[1]   Time-dependent buoyant plumes form at the outflow of tidally dominated estuaries. When estuary discharge velocity exceeds plume internal wave speed c, a sharp front forms at the plume's leading edge that expands from the time-dependent source. Using observations of the Columbia River tidal plume from multiple tidal cycles we characterize time-evolving plume structure and quantify front speed U_f, plume internal wave speed c, front curvature, and ultimate extent. We identify three distinct stages of propagation: (1) Initially, the plume is strongly influenced by shallow bathymetry near the river mouth. (2) As the front advances offshore the plume detaches from the bottom and expands as a freely propagating gravity current with relatively constant U_f, c and frontal Froude number $F = U_f/c$. Ambient currents explain intracycle variability in U_f and winds alter front shape. Variability in ambient stratification associated with previous cycles' plume remnants leads to complex fronts and internal waves. (3) Finally, the plume decelerates, adjusts toward geostrophy, and may radiate additional internal waves. Using a simple kinematic model, we suggest that constant frontal propagation speed, $U_f = 0.9 \pm 0.1$ m/s, during stage 2 is primarily controlled by linearly increasing volume flux from the Columbia River mouth. As this discharge rate subsides, the plume expands as a fixed volume with decreasing front speed (stage 3). The plume's final extent is controlled by the Rossby radius, which scales with a length based on the total volume discharged. This provides an integral description of plume front evolution based on the time-dependent estuary discharge.

1.   Introduction

[2]   Over the last half century considerable scientific effort has been devoted to regions of freshwater influence, those parts of the oceans whose physical, biological and chemical properties are strongly affected by river input [*Simpson*, 1997]. This effort has focused in two distinct domains: the estuary [e.g., *Jay and Smith*, 1990] and the far-field river plume [e.g., *Fong et al.*, 1997].

[3]   Estuaries are the domain in which fresh river water first encounters sea water. Their dynamics are largely determined by the competition between tidal stirring/mixing and freshwater input from upstream [*Hansen and Rattray*, 1966; *Bowden and Gilligan*, 1971; *Jay and Smith*, 1990; *Nash et al.*, 2009]. Far-field plumes are low-salinity mesoscale features that disperse river water across coastal margins. Their dynamics are dominated by buoyancy, planetary rotation and wind forcing [*Yankovsky and Chapman*, 1997; *Fong and Geyer*, 2002; *Hickey et al.*, 2005]. As interest in these domains has grown, so has attention to the processes that connect them. *Horner-Devine et al.* [2009] conceptualized four dynamic regimes: the source (i.e., estuary), tidal plume, recirculating plume [*Yankovsky and Chapman*, 1997; *Horner-Devine*, 2009] and far-field plume. This work focuses on the tidal plume.

[4]   Fed by the ebb discharge from a river mouth, a tidal plume is an expanding volume of buoyant fluid that spreads offshore along the ocean surface. The dynamics and characteristics of tidal plumes are distinct from both estuaries and far-field plumes. In contrast to far-field plumes, they are highly time dependent (tidally modulated), much smaller scale, and their dynamics are, at least initially, independent of the earth's rotation [*Garvine and Monk*, 1974]. In contrast to estuaries, tidal plumes are not constrained by a river channel so are highly three-dimensional. Throughout this work we use the terms "plume" and "tidal plume" interchangeably and distinct from the larger-scale "far-field plume."

1.1.   Tidal Plume Fronts

[5]   Some of the earliest observations of tidal plume fronts were made at the Connecticut River mouth. *Garvine and Monk* [1974] identified "vigorous" convergence at the horizontally propagating plume front and determined that propagation was driven by the cross-front density gradient.

[1]College of Oceanic and Atmospheric Sciences, Oregon State University, Corvallis, Oregon, USA.

Isopycnals were displaced downward in the $O(50\text{ m})$ wide front. Inshore of it they were shallower and horizontal.

[6] *Luketina and Imberger* [1987, hereafter LI87] described the liftoff and radial expansion of the tidal plume that formed from the discharge of a small estuary into Koombana Bay, Australia. That work described frontal structure as rotary circulation around a turbulent core [see LI87, Figure 2]. *Marmorino and Trump* [2000] document further evidence of this head structure in the Chesapeake Bay plume. In the Columbia River tidal plume's front, intense turbulence and large vertical displacements support LI87's diagram of frontal structure [*Orton and Jay*, 2005]. Throughout these studies it has been clear that these fronts propagate as buoyant gravity currents.

[7] Beyond the mouth LI87 described the following two regimes: (1) a surface buoyant jet whose cross-shore extent moved steadily offshore as ebb discharge through the mouth strengthened and (2) a buoyant plume that expanded radially from the location of the jet's extent. This resulted in a total front propagation speed that was the sum of the jet extent translation speed and the plume spreading rate.

1.2. Gravity Currents

[8] In his seminal work on gravity currents, *Benjamin* [1968] proposed that the frontal Froude number

$$F = \frac{U_f}{c}, \tag{1}$$

should be an order one function of the nondimensional layer depth (ratio of plume thickness, h, to the full water depth, d). Here U_f is the gravity current front's speed relative to the ambient fluid and c is the first-mode long-wave speed within the plume. In the deep water limit, Benjamin predicted, $F = \sqrt{2}$. More recently, in a lock-release framework, *Shin et al.* [2004] have proposed that $F = 1$ is the most appropriate value for deep water gravity currents. Regardless of the debate regarding the specific value of F, LI87 and *Marmorino and Trump* [2000] observe F to be roughly constant and $O(1)$ (throughout this work, $O(\ )$ is used to indicate the order of magnitude of the quantity in question).

1.3. Tidal Plume Models

[9] In an effort to dynamically model a time-dependent plume, *Garvine* [1984] assumed a radially spreading flow with steady source conditions. Garvine simplified the plume dynamics to a two-layer system involving the shallow water wave equations and assumed the front propagated as a gravity current (he used a $F = \sqrt{2}$ frontal condition). More recently, *Jay et al.* [2010] formulate a model that conserves mass, momentum and buoyancy in a quasi-steady, front-following frame. Rather than prescribing the frontal Froude number, *Jay et al.* [2010] explore the effect of different mass and momentum entrainment mechanisms on frontal evolution. Both models predict the plume front to propagate offshore with initially high deceleration that decreases offshore (i.e., front speed decreases rapidly, then more slowly).

[10] Rapid deceleration conflicts LI87's observation that $U_f \approx$ Constant. Using *Chen*'s [1980] kinematic plume model (with $F =$ Constant frontal condition), LI87 found that roughly constant frontal propagation speeds could be explained if the volume flux through the mouth (the estuary discharge) increased linearly in time during the initial phase of the tidal cycle, a condition approximately observed. LI87's agreement between modeled and observed U_f evolution suggests the time dependence of the source discharge may be more important than both the dynamics of the plume interior [*Garvine*, 1984], and the details of frontal dynamics [*Jay et al.*, 2010] in predicting plume front motion.

1.4. Outline

[11] This work describes the structure and explores the dynamics of the Columbia River tidal plume and front. While the Columbia plume is much larger than the small rivers in the above studies, there remain important similarities. For example, the Columbia River tidal plume source is highly supercritical, time dependent and produces a strong front [*Orton and Jay*, 2005]. In less than 8 h this plume spreads estuary fluid greater than 20 km offshore where it becomes strongly influenced by planetary rotation [*McCabe et al.*, 2008]. Our observations capture front evolution from a bottom interacting regime through plume expansion to the tidal plume's ultimate adjustment toward geostrophy.

[12] In section 2 we describe the physical and environmental setting of the observations and the measurements. Section 3 begins with a description of front shape and basic plume structure. Sections 3.3 and 3.4 describe the evolution of simple and complex fronts, respectively. The interebb variability and intraebb evolution of plume structure and front speed, as well as estuary discharge are presented in section 4. In section 5 we employ *Chen*'s [1980] kinematic model to relate the evolution of front speed to the observed time dependence of the estuary discharge. Like LI87, we identify a regime of roughly constant U_f associated with the linearly increasing estuary discharge. We extend LI87's analysis to a "relaxation" regime, brought about by decreasing estuary discharge, during which the plume expands as a fixed volume and approaches geostrophic balance. Results and implications are summarized in section 6.

2. Setting and Data

[13] The Columbia River flows into the Pacific Ocean from between the states of Washington and Oregon, United States (Figure 1). Constricted by two jetties, the estuary narrows from 10 to 3.5 km at the mouth and discharges its fluid westward into the relatively unbounded coastal ocean. Within 8 km of the mouth is a relatively flat, shallow (water depth, $d \approx 20\text{ m}$) region that is roughly radially symmetric about the tip of the north jetty; we refer to this as the "bar region." The 20 m deep shipping channel, which runs from the river mouth to the southwest, is the primary exception to this symmetry (also, there is a 20 m deep dredge pile at $(x, y) = (-8, 0)$ km). Offshore of the bar region, the water depth increases rapidly from 20 m to >60 m in only 2 km (Figure 1a).

[14] The origin of our chosen coordinate system is at 46.24° N, 124.08° W, with the positive x, u and y, v directions eastward and northward, respectively (Figure 1b). The coordinate system is approximately aligned with the mean river discharge, perpendicular to the north-south coast, and has origin just north of the south jetty. z is defined as positive upward from the ocean surface.
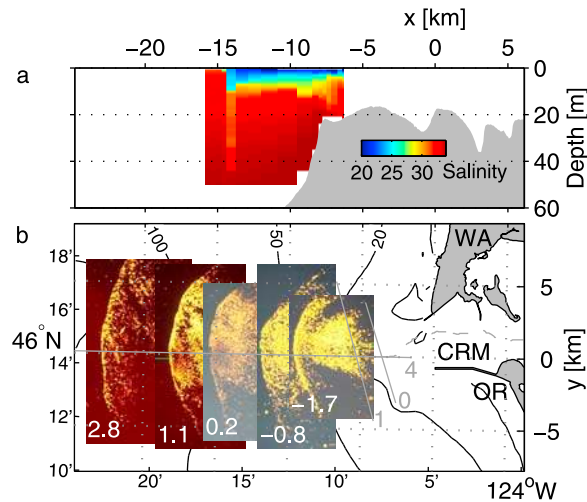
Figure 1. Setting at the Columbia River mouth (CRM). (a) Water depth and plume salinity at low tide ($t = 0$) during the second ebb of 9 August (aug09b). (b) Images of the ship's X band radar (white numbers indicate time relative to low tide (t) in h) show the propagation of the front in Figure 1a. Also shown are depth contours (black; m) and transect lines (solid gray); the axes indicate the x, y coordinate system. In Figure 1a, water depth follows line 4 for $x < -4$ km and the shipping channel (dashed line in Figure 1b) for $x > -4$ km.

2.1. Sampling

[15] In August 2005, seven "front-tracking" experiments were performed from the R/V *Pt. Sur* as part of the River Influences on Shelf Ecosystems (RISE) study [*Hickey et al.*,

2010]. During each tidal cycle approximately 8–15 E-W transects across the front were obtained as it propagated offshore (Figure 2a). This was continued until the front was no longer a clear feature in the observations or when the ship returned inshore to catch the next ebb pulse. Each experiment is denoted by its "tidal ID" which is composed of the three letter month prefix ("aug") followed by its numeric day of August, followed by an "a" or "b" to denote the first or second ebb of that day, respectively. Repeated "Cross-mouth" transects, along lines 0 and 1 and over complete tidal periods (Figure 1b), resolved the cross-mouth structure and time dependence of estuary discharge. All transects were obtained at ship speeds of 4–6 knots.

2.2. Environmental Conditions

[16] During our sampling, winds were mild, variable, and predominantly upwelling favorable (Figure 2b). Moderate winds ($O(5$ m/s)) were experienced during ebbs aug22a, aug22b and aug25b. River flow in August was low, ≈ 4000 m^3/s, compared to peak freshet values in excess of 10,000 m^3/s [*Hickey et al.*, 2010]. Tidal elevations η, as computed from XTide (D. Flatter, XTide version 2.9.5, 2007, available at http://www.flaterco.com/xtide/) for the "Columbia River, N. Jetty" exhibit both a strong spring/neap modulation and variable diurnal inequality. We quantify the tidal drop $\Delta\eta_\circ$ for a given ebb as

$$\Delta\eta_\circ = \eta_{high} - \eta_{low}, \tag{2}$$

where η_{low} is the tidal height minimum and η_{high} the preceding maximum (Figure 2c). Front tracking experiments capture a range of $\Delta\eta_\circ$ from 1.1 to 2.8 m. The strength of the
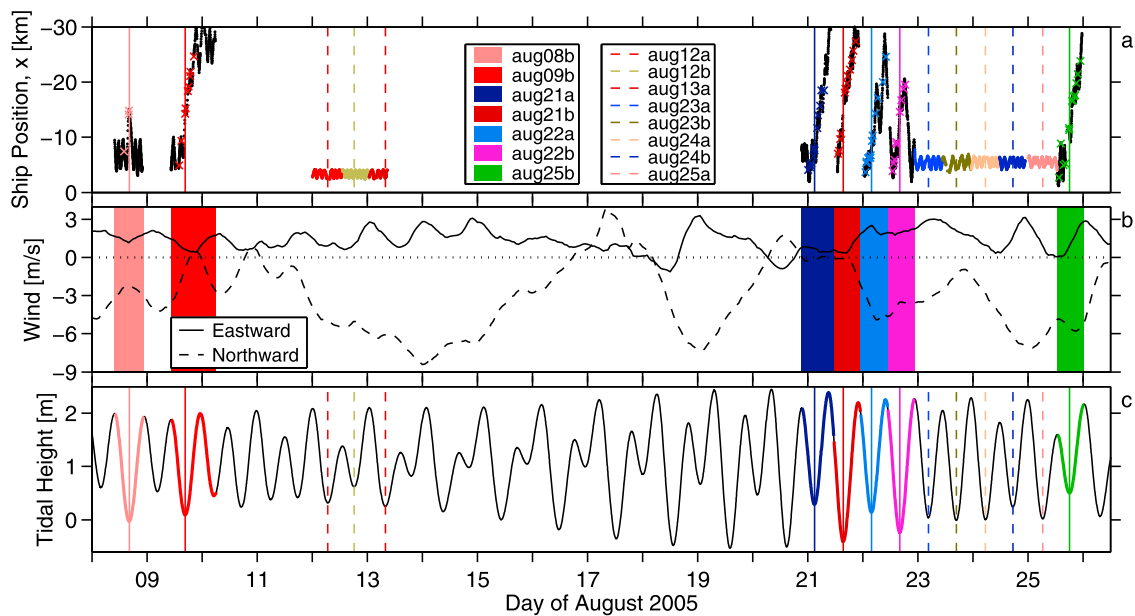
Figure 2. (a) Cross-shore location of Chameleon sampling (black) and plume fronts (color crosses; left legend). Colored lines represent cross-mouth sampling (right legend). (b) The 10 h low passed wind speed from National Data Buoy Center buoy 46029 (Columbia River Bar). (c) Tidal height from XTide with time periods of each front tracking experiment in color. Vertical lines in Figures 2a and 2c (solid for front tracking and dashed for cross-mouth sampling) indicate the reference time (t_{low}) of the tidal cycle.

diurnal inequality is represented by $\Delta\eta_{\circ} - \Delta\eta_{-1}$, where $\Delta\eta_{-1}$ is the prior ebb's tidal drop. For each experiment, time

$$t = \hat{t} - t_{low}, \tag{3}$$

is referenced to the time of low tide, t_{low}, of the given ebb, where $\hat{t}$ is chronological time (Figure 2c).

2.3. Instrumentation

[17] This work combines microstructure profiler measurements, shipboard acoustics and surface backscatter from X band radar to capture the evolving internal plume structure and plan view front shape.

[18] Two RD Instruments acoustic Doppler current profilers (ADCPs) were used throughout this cruise. A hull-mounted 300 kHz instrument measured velocities from 4.5 down to 100 m below the surface in 1 m bins. A 1200 kHz instrument mounted 1.4 m below the surface on a pole alongside the ship provided lower noise velocity estimates in 0.5 m bins from 2.2 to 24.2 m depth. This data was preferred between $0 > z > -20$ m. Both ADCPs bottom tracked and used 1.5 s averaging intervals. A linear fit across data between 2.2 and 4.7 m depth was used to extrapolate 1200 kHz velocity data to the surface. A 120 kHz Bio-sonics™ acoustic echo sounder was mounted on a second pole 1 m below the surface and recorded profiles of acoustic backscatter from zooplankton and turbulence every 0.5 s in 0.017 m bins.

[19] Vertical profiles of conductivity, temperature, pressure, optical backscatter, velocity shear and temperature gradient were obtained every 1–3 min with the Chameleon microstructure profiler [Moum et al., 1995]. At this profile rate and ship speed, horizontal resolution was 100–500 m. Free falling at 1 m/s, Chameleon provides data with roughly 1 cm vertical resolution. Turbulent kinetic energy (TKE) dissipation rate, ε, was calculated in 1 m depth bins by fitting theoretical shear spectra to observed spectra from Chameleon's shear probes [Moum et al., 1995]. Estimates of ε were not obtained above 3 m depth because the profiler was accelerating and changing orientation. Furthermore, contaminated ε data were identified when the ship orientation, drift and water column shear combined to place the profiler in the ship's wake; this affected data, for short periods, down to 9 m depth.

[20] Images from the ship's X band radar (e.g., Figure 1b), tuned to detect surface roughness, were captured every 2 min. Bands of high radar backscatter intensity correspond with regions of surface velocity convergence [Alpers, 1985; Marmorino et al., 2004]. Bands were traced and indexed by hand then transformed into the earth's frame. These traces provide front position, shape and orientation as a function of time.

2.4. Front Identification

[21] Because it is not always clear what internal feature a given band of elevated radar backscatter represents, it was necessary to use internal measurements to identify fronts. In general, front locations were identified objectively as the location of maximum horizontal velocity convergence at $z = -2.35$ m. For well formed fronts, this also corresponds to the near-surface salinity gradient maximum $(\frac{\partial s}{\partial x})_{max}$ at $z = -1.5$ m and the frontal locations identified from echo sounder and

radar backscatter. When multiple or ambiguous fronts existed, it was necessary to use a salinity threshold to identify primary fronts and differentiate these from secondary fronts, which represented propagating wave-like disturbances either ahead or behind the main front (see auxiliary material for more detail).[1] When even this failed, front locations were interpolated between neighboring realizations. Ambiguity estimates were assigned subjectively to include all front locations that would be identified by alternate reasonable criteria. When fronts were simple and distinct these methods produced identical results (ambiguity is small). However, when frontal structure was complex (section 3.4) these methods produce different results and front position ambiguity is large.

[22] Front position, x_f, is defined as the intersection of the front with the x axis at $y = 0$. In cases where the front was identified away from the x axis (experiments aug22b, aug25b), front locations were translated to the x axis using radar estimates of front shape. This makes x_f a consistent variable for interebb comparisons and minimizes error associated with radar derived front location estimates.

[23] Based on these data, front speed is estimated as

$$U_f^* = \frac{\Delta x'}{\Delta t}, \tag{4}$$

where Δt and $\Delta x'$ are the time and cross-front distance between realizations, respectively. Here $\Delta x' = |\Delta x| \cos \phi$, where $|\Delta x|$ is the magnitude of the vector connecting consecutive realizations of front position (x_f, y_f), and ϕ is the angle between this vector and the front-normal direction, determined from radar backscatter data (both vectors pointed generally westward). The velocity error upper bound was calculated by differencing front position ambiguity minima in one realization of front position from ambiguity maxima in the next, and vice versa for the lower bound.

3. Plume Front Structure and Evolution

3.1. Front Shape and Evolution

[24] A defining characteristic of the Columbia River tidal plume is its time dependence. On each ebb, the pulsed discharge from the mouth generates a tidal plume that spreads offshore. Traces of front position illustrate this in plan view for 5 ebbs (Figure 3). (Ebbs aug08b and aug21a have been omitted from Figure 3. Traces of front aug08b are similar to those of aug09b until $t \approx 1$ h at which time the ship returned inshore and the front was out of range of the radar. Due to wind and surface wave conditions many fronts were not resolved as clearly as aug09b. In particular front aug21a was nearly unidentifiable in radar images. Because of this incomplete and poor sampling these ebbs are not presented in Figure 3.)

[25] The second ebb of 9 August (aug09b) demonstrates plume-front evolution during a period of weak winds (Figure 3a). Four h prior to low tide the front emerged from the estuary mouth. At this time it was "S" shaped and attached to the north jetty. Initially, the front propagated

---
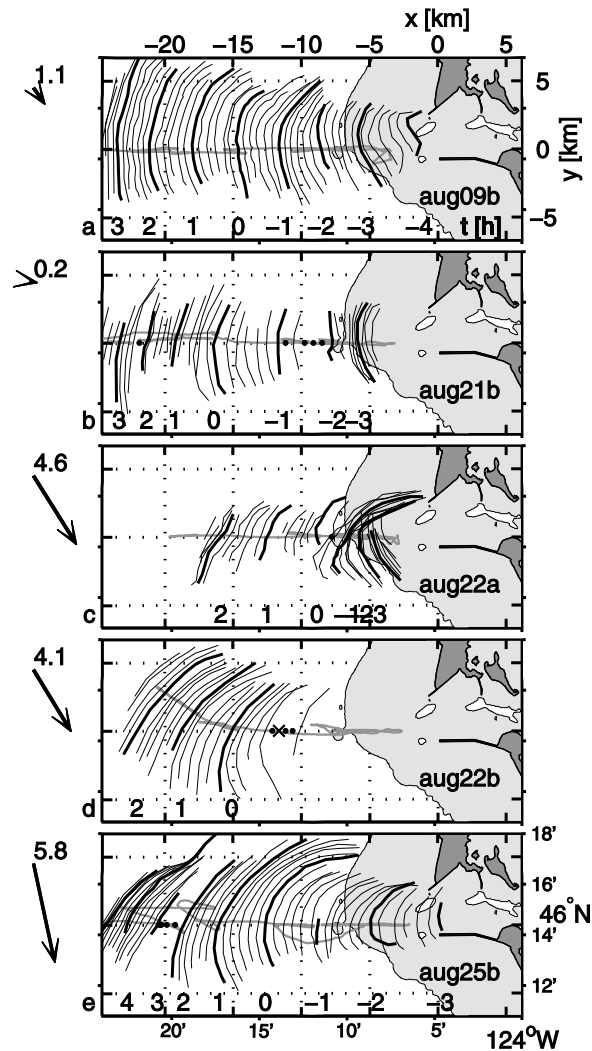
Figure 3. Traces of front location from radar images during five ebbs (ebb identification is in the lower right corner). Numbers along the bottom indicate the h (relative to low tide (t)) of thick line traces. Thin lines are traces every 10 min. Where there are gaps in trace data, missing thin lines are marked by dots and thick lines by crosses. The coordinate system is labeled at upper right (inward tick marks, grid). The coastline is shaded dark and depths shallower than 23 m are lightly shaded. A gray line shows the ship's track. Mean wind, during each period, from buoy 46029 is indicated by the arrow at left (numbers indicate magnitude in m/s).

rapidly, as seen by large spacing between traces near $x = -4$ km. During the next 15 km ($-5 > x > -20$ km) uniform trace spacing indicates constant, though slower, front speed. Throughout this time, increasing radius of curvature of traces suggests that the plume expanded radially. The centroid of expansion was near the x axis so that the plume front was approximately normal to our ship track. Tighter trace spacing beyond -20 km indicates front deceleration, after which the band of elevated radar backscatter was no longer visible.

[26] Like aug09b, front aug21b emerged under weak wind conditions and was essentially perpendicular to the x axis as

it propagated offshore (Figure 3b). Between $x = -7$ and -16 km (-2 to 0 h) this front propagated offshore more rapidly than any other. It then decelerated suddenly, released a nonlinear internal wave (NLIW) [i.e., *Nash and Moum*, 2005], and moved more slowly offshore over the remaining 8 km. This rapid deceleration is explored further in section 4.3.

[27] In contrast to the north-south symmetry of aug09b and aug21b, fronts aug22a, aug22b and aug25b propagated obliquely to the x axis (Figures 3c–3e). We attribute this asymmetry and associated plume deflection to the ≈ 5 m/s wind that was blowing to the south during these periods, contrasting the weak winds during aug09b and aug21b. However, the magnitude of the plume's deflection exceeds that predicted by a wind-forced slab model, suggesting that wind-induced surface currents may also contribute to plume shape and curvature.

[28] Timing of frontal emergence, relative to low tide, varied from ebb to ebb and was uncorrelated with the wind. For example, front positions at low tide ($t = 0$) during ebbs aug22a and aug22b (similar wind conditions) were $x = -7$ km and -15 km, respectively. The relationship between front timing and the diurnal inequality is presented in section 4.5.

3.2. Plume Anatomy at Peak Ebb

[29] We begin by describing the large-scale internal structure of a "classic" plume and gravity current front that resulted from propagation through a relatively homogeneous coastal environment (Figure 4). This front formed on the greater ebb of 8 August ($\Delta\eta_\circ - \Delta\eta_{-1} = 0.8$ m), during spring tides ($\Delta\eta_\circ = 2.0$ m) and weak and steady upwelling winds (Figure 2). It exhibited symmetrical spreading similar to aug09b (Figure 3a), but was not tracked past $x = -15$ km. At the time of frontal crossing, at $x = -14$ km, the front was moving offshore at $|U_f^*| = 0.96$ m/s. The plume structure is most clearly visualized by elevated acoustic backscatter and shear squared, $S^2 = (\partial u/\partial z)^2 + (\partial v/\partial z)^2$ (Figures 4a and 4b), which have much higher horizontal resolution than Chameleon profile data. Density profiles in (b) clearly distinguish plume waters, which were often >10 kg/m^3 lighter than the ambient. Stratification, $N^2 = -g\rho_\circ^{-1}\partial\rho/\partial z$, can be inferred from the slope of density profiles. Coincidence of maximum N^2 and S^2 suggests S^2 is a useful representation of plume structure. Offshore of $x = -8$ km, the overarching plume structure is that of a typical buoyant gravity current: led by a front, light fluid flows along the surface of a relatively motionless and denser ambient.

[30] Within this overarching structure, the following five regions of distinct internal structure are identified in Figure 4: (1) liftoff, (2) transitional plume, (3) two-layer plume, (4) front, and (5) ambient.

[31] 1. The liftoff region extends from the river mouth across the bar region ($x > -7.7$ km) and is characterized by intense shear and turbulent dissipation throughout the water column. Throughout this region, the flow is supercritical, i.e., the depth mean fluid speed is greater than the first-mode internal wave speed. In this example, bands of high S^2, associated with the plume base, connect to the bottom at two locations ($x \approx -5.2$ and -7.7 km), producing intense turbulent dissipation, ($\varepsilon > O(10^{-5}$ W/kg)), high bottom stress and sediment resuspension [*Spahn et al.*, 2009]. These
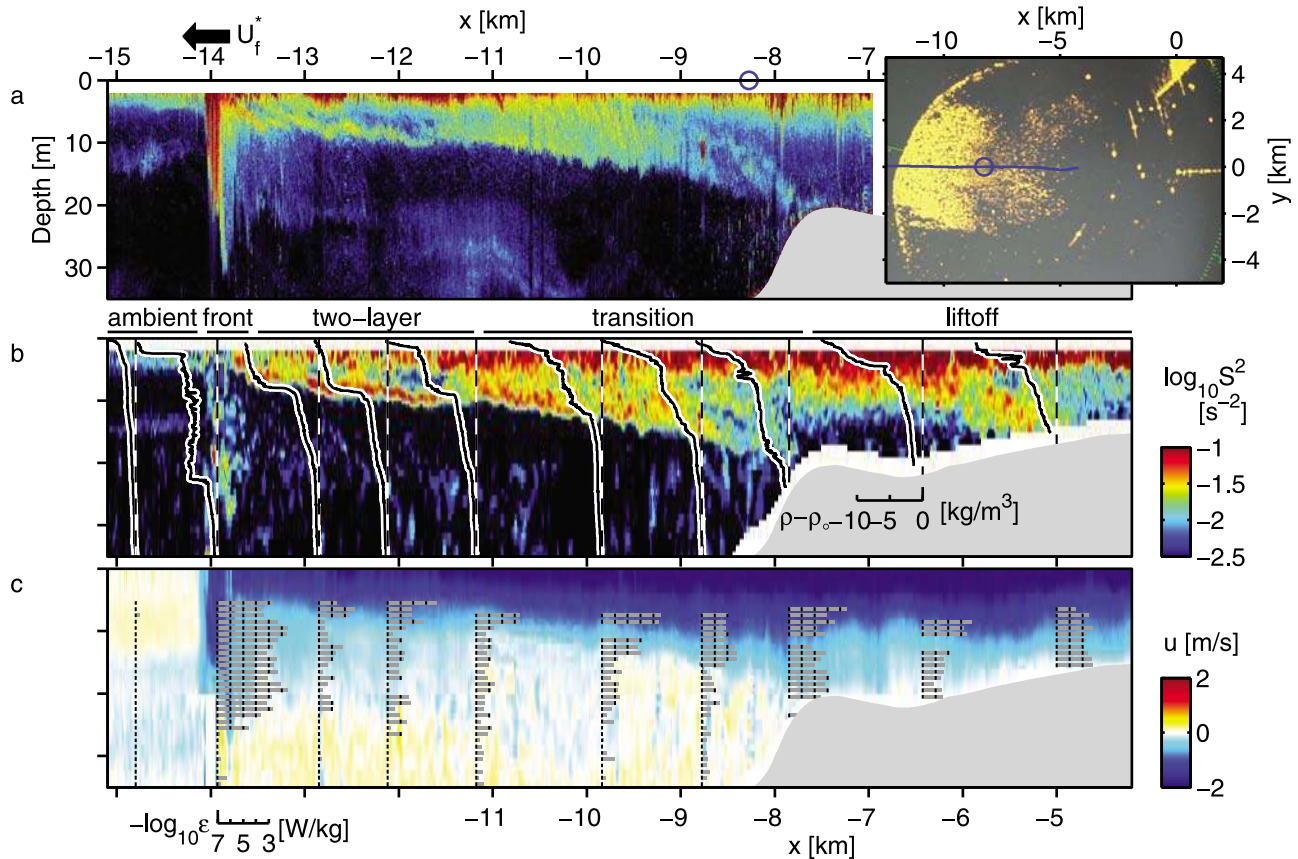
Figure 4. Internal plume structure for a moderate ebb near low tide (aug08b; $\Delta\eta_\circ = 2.0$ m and $t = -0.3$ h at frontal crossing). (a) The 120 kHz acoustic backscatter. (b) Log of shear squared (color) and vertical profiles of density deficit $\rho - \rho_\circ$ (black lines; $\rho_\circ = 1026.3$ kg/m³). (c) Eastward velocity (color) and $\log_{10}\varepsilon$ (gray bars; tick marks indicate decades above 10^{-7} W/kg). Roughly 1 in 5 vertical profiles are shown. An X band radar image (inset) shows plume extent when the ship was at $x = -8.3$ km (circle); blue line indicates ship track. This transect was acquired over the 1 h period 1508–1610 UT 8 August 2005 as the ship traveled west at 6 knots.

multiple attachment/detachment points are associated with individual liftoffs, which may result from (1) the flow disconnecting and reconnecting as it moves across the complex bathymetry, (2) the liftoff of an intermediate layer of plume fluid, or (3) the space-time aliasing inherent in our sampling. We also note that this liftoff region is not static, but moves in and out of the estuary with the tidal cycle; this snapshot is characteristic of its most seaward extent during peak ebb.

[32] 2. The "transition" region occurs offshore of liftoff and inshore of $x = -11.3$ km. Here, S^2 and N^2 are high throughout the plume and TKE dissipation in the plume base ($\varepsilon = O(10^{-4}$ W/kg)) exceeds background levels by a factor of 1,000. We consider this a transition region because the flow appears to have "memory" of its bottom-interacting state (i.e., strongly sheared as in the liftoff region but no longer connected to the bottom). In addition, this region is considered transitional in that it rapidly thins from 20 m when bottom interacting to 10 m. Surface velocities $|u(0)| > 2$ m/s exceed the front speed by more than a factor of 2, which, combined with the strong vertical salinity gradient, efficiently supplies buoyant estuary fluid offshore toward the front. Numerous unstable overturns were observed in

this region, such as that at $x = -8$ km at 7 m depth with $\varepsilon = O(10^{-5}$ W/kg). Offshore of this, at nearly the same depth, a layer of weak stratification (profiles at -9.8 and -8.8 km) is observed, likely a result of mixing.

[33] 3. Offshore of the transition region and inshore of the front ($-13.5 < x < -11.3$ km) the plume had developed into a more well-mixed, two-layer flow (S^2 and N^2 were concentrated at the plume base). Turbulence was strong in the plume base ($\varepsilon = O(10^{-5}$ W/kg)) but a lack of ε estimates in the surface (due to contamination by the ship's wake) inhibits comparing the detailed turbulent structure of this region to others.

[34] 4. The front is a narrow region of large surface density and velocity change at the outer edge of the plume ($-14.1 < x < -13.5$ km). Surface density changes by >9 kg/m³ across the front and horizontal convergence at the front's leading edge is intense (u changes by >1 m/s in <100 m). This forces fluid downward at >0.5 m/s. Along the inshore side of the front upward velocities are >0.3 m/s, providing the return circulation for the turbulent rotor and "head" wave, as described by LI87. The head height, h_f, is the maximum isopycnal displacement through the front relative to the ambient fluid ahead of it, and often exceeds 20 m (h_f

is distinct from the plume thickness, h, defined as the depth of the 30 salinity contour inshore of the front). Shear within the front is not well resolved, possibly due to small scales of variability relative to the ADCP footprint. A thin surface layer, $z > -2$ m, of light fluid has been supplied to the front by the convergent flow. Below this, overturns of multiple scales are apparent in the density profile and TKE dissipation was extremely vigorous ($\varepsilon > 10^{-3}$ W/kg).

[35] 5. The ambient region offshore of the front provides context for the in-plume observations ($x < -14.1$ km). At this time, ambient water is flowing weakly onshore ($u < 0.3$ m/s) at the surface, and weakly offshore below 13 m depth. This fluid is much less stratified, sheared and turbulent ($\varepsilon < 10^{-7}$ W/kg) than within the plume.

[36] The aggregate structure of these regimes portrays a plume structure that is in many ways similar to the smaller-scale plumes described by LI87 [Figure 2], *Garvine* [1974], and *Marmorino and Trump* [2000] in which an offshore propagating front with a "turbulent core" in its head wave, is fed by a two-layer surface flow that exceeds the front speed. In addition, we identify a transitional region associated with the thinning of highly sheared and stratified fluid that was recently interacting with the bottom, similar to *Garvine*'s [1984] supercritical "steady flow" regime (inshore of his "trailing front") and *MacDonald and Geyer* [2004] and *MacDonald et al.*'s [2007] "liftoff zone." This region may be considered analogous to LI87's "jet" regime.

[37] Some distinctions between the above regimes are elucidated by considering wave speeds of long first-mode internal waves as computed from the Taylor-Goldstein equation using the full density and velocity profiles in the geographic reference frame [*Drazin and Reid*, 2004]. For example, within the liftoff region, the flow is supercritical (i.e., all disturbances propagate offshore). Thus, during peak ebb, information can be transmitted through the liftoff region to the plume, but not the other way around (the estuary controls the plume). In contrast, in the transition and two-layer regions, internal waves may propagate in either direction (phase velocities of offshore propagating waves are ≈ 1.5 m/s, while those propagating onshore are $\lesssim 0.5$ m/s). At the front, a discontinuity exists; offshore propagating waves behind the front can catch up to it (their wave speeds exceed the front speed), but cannot propagate ahead of it into the ambient where the wave speed (<0.4 m/s) is lower than the front speed (≈ 1 m/s). Thus, at this time, dynamics at both the front and liftoff region can influence the plume between them, but not beyond. At the same time, because these locations act as barriers to internal wave propagation, they are locations where wave energy can build up or dissipate.

[38] The location of plume liftoff appears to be strongly linked to topography, and is consistent with *Jones et al.*'s [2007] transition of a supercritical buoyant discharge to buoyancy driven (plume) dynamics. They define a "jet-to-plume" length scale

$$L_M = \frac{U_\circ a^{1/4}}{(g_\circ')^{1/2}}, \qquad (5)$$

where a is the cross-sectional area of the mouth, $U_\circ$ the mean velocity through it, and $g_\circ'$ the reduced gravity. Appropriate values for the Columbia River are $a = 60,000$ m^2,

$U_\circ = 2$ m/s (peak ebb) and $g_\circ' = 0.07$ m/s^2 (typical of August 2005). These values give $L_M = O(100$ m). *Jones et al.* [2007] explain that L_M can only be interpreted as the horizontal scale for jet-to-plume transition if

$$d \geq L_M/3. \qquad (6)$$

Thus, the discharge from the Columbia River mouth should interact strongly with the bottom until the water depth exceeds 30 m. Offshore of this the flow is expected to behave as a plume/gravity current (i.e., driven by its buoyancy). Our observation that the flow interacts with the bottom until $x \approx -8$ km (Figure 4) is thus consistent with (6), and suggests that the liftoff location is connected to bottom depth variability.

[39] While it is tempting to interpret the basic structure represented in Figure 4 as being typical, this is a single pseudosnapshot (obtained as the ship moved offshore and the flow evolved slightly) of a "simple" plume. In practice, we observe plume evolution to be strongly influenced by the following two factors: temporal variability and spatial complexity.

[40] 1. Nearly all the features of the flow (detachment point, front location, plume thickness, shear/stratification structure, turbulence, and flow direction) are controlled by the tidally variable upstream flow rate (estuary discharge). This causes these variables, and the plume in general, to be highly time dependent and rapidly evolving.

[41] 2. In contrast to the distinct front in Figure 4 (which propagated through a relatively homogeneous coastal environment) most fronts exhibited a significant amount of spatial complexity. This complexity arises because the composition of plume source water changes in time and coastal waters are often "contaminated" with tidal plume remnants from previous tidal cycles.

[42] In section 3.3, we describe the time evolution of a simple tidal plume front with initial structure similar to that of Figure 4. This is contrasted (section 3.4) with the evolution of two complex fronts, which, from our limited sampling, are more typical of the norm than the exception.

3.3. Plume Evolution I: A Simple, Distinct Front

[43] The evolution of the internal structure of front aug09b is summarized as a sequence of pseudosnapshots in Figure 5. This front, generated by a greater ebb during spring tides and weak winds (Figure 2), resulted in a highly symmetric frontal expansion (Figure 3a) with colocated frontal signatures in shipboard radar, density, velocity and TKE dissipation.

[44] In its early stages (prior to Figure 5a and $t = -2$ h), the front was over the bar and the four plume regions identified in Figure 4 were not distinct. Instead, the plume and its front both strongly interacted with the bottom. In Figure 5a, this topographic influence was still evident as rapid thickening and enhanced ε at $x - x_f = 4$ km, possibly associated with a hydraulic transition. In the following, we focus on the later time period when the plume front is freely propagating.

[45] Initially (Figure 5a), frontal displacements h_f are small, similar to the plume thickness behind the front. This may result because the front was recently constrained in amplitude by the shallow bar, and has had limited time for growth. As the plume evolved (Figure 5a to Figure 5b), h_f
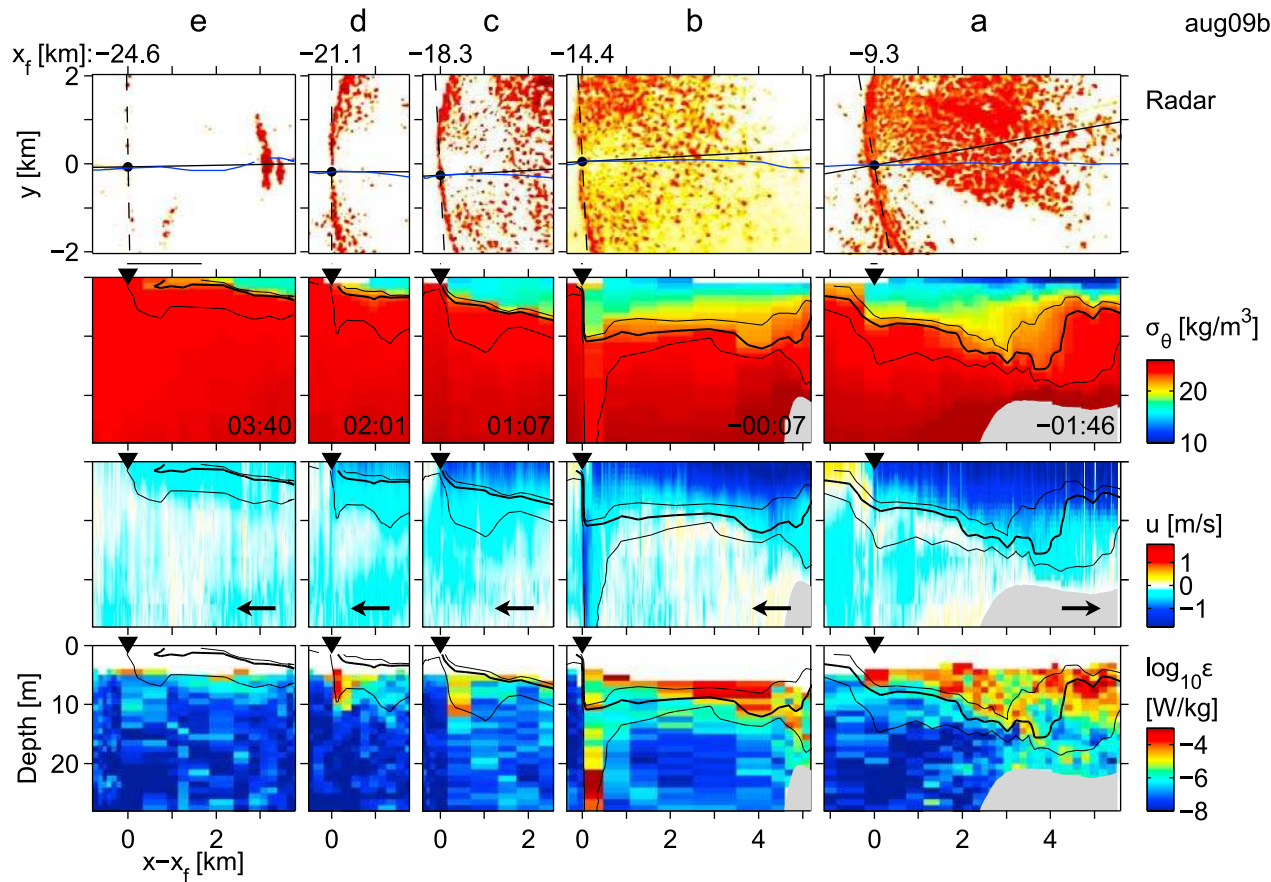
Figure 5. A time sequence of east/west transects along line 4 through the front generated during the second ebb of 9 August (aug09b). Plots are in reverse chronological order and move progressively offshore from right to left. Horizontal axes have been corrected for Doppler shifting, so preserve distance relative to the moving front (but distort distances relative to topography). Radar image intensity, cross hairs indicate front orientation. The blue line indicates the ship's track. Potential density (σ_θ). Eastward velocity (u). Arrows show the direction of ship travel. TKE dissipation ($\log_{10}\varepsilon$). Front location, x_f, and time t, of frontal crossing (relative to low tide) are indicated for radar and σ_θ. For σ_θ, u, $\log_{10}\varepsilon$, the 28, 30 (thick), and 32 salinity contours are shown. Black triangles and line segments (above triangles in σ_θ plots) indicate frontal location and its position ambiguity.

grew rapidly to >30 m. However, in just 75 min, the front decayed by a factor of 3 to less than 10 m (Figure 5b to Figure 5c). Based on the observed dissipation rates within the front ($\varepsilon \approx 10^{-3}$ W/kg) and the mean mechanical energy within the head of 2 J/kg (APE+KE; see *Moum et al.* [2007] for method used), turbulence dissipation could erode the front in 30 min. Thus, NLIW radiation [i.e., *Nash and Moum*, 2005] is not needed to account for the observed decay in h_f. Ultimately, h_f and surface convergence weakened further (Figure 5c to Figure 5e), so that shipboard radar no longer resolved the front.

[46] In contrast to h_f, which first grew then decayed in amplitude, plume velocity u, and thickness h (defined as the depth of the 30 salinity contour (thick contour in Figure 5, σ_θ, u, and $\log_{10}\varepsilon$ plots)) decreased monotonically. During this time, plume density was relatively constant (8 ± 1 kg/m^3 lighter than ambient).

3.4. Plume Evolution II: Complex Fronts

[47] The frontal evolution of the remaining five plumes was much more complex than the simple structure described in sections 3.2 and 3.3. The front generated by ebb aug22a (Figure 6) illustrates many characteristics of complex fronts, which are generally associated with lateral variability of the stratification of the receiving waters (due to the presence of remnant tidal plume fluid). This front was generated by a lesser ebb during spring tides ($\Delta\eta_\circ = 2.1$ m) and weak winds.

[48] Initially the front is identified as the region of strong surface convergence and intense top-to-bottom turbulence (Figure 6a). At this time the estuary fluid inshore of the front is denser than the "remnant plume" fluid offshore of it. We term this counterintuitive arrangement a "reverse front." Inshore of the reverse front velocity is maximum at the surface, $\approx$2 m/s, and shear is strong throughout the water column. Offshore of it, fluid speeds are maximum below the remnant plume. Thus, the denser water issuing from the estuary is forced to flow beneath the more buoyant remnant plume. Intense dissipation ($\varepsilon = O(10^{-3}$ W/kg)), possibly a result of convective instability, occurs at the frontal discontinuity ($x - x_f = 0$ km) where dense surface waters are driven into the buoyant remnants. Reverse fronts (in which
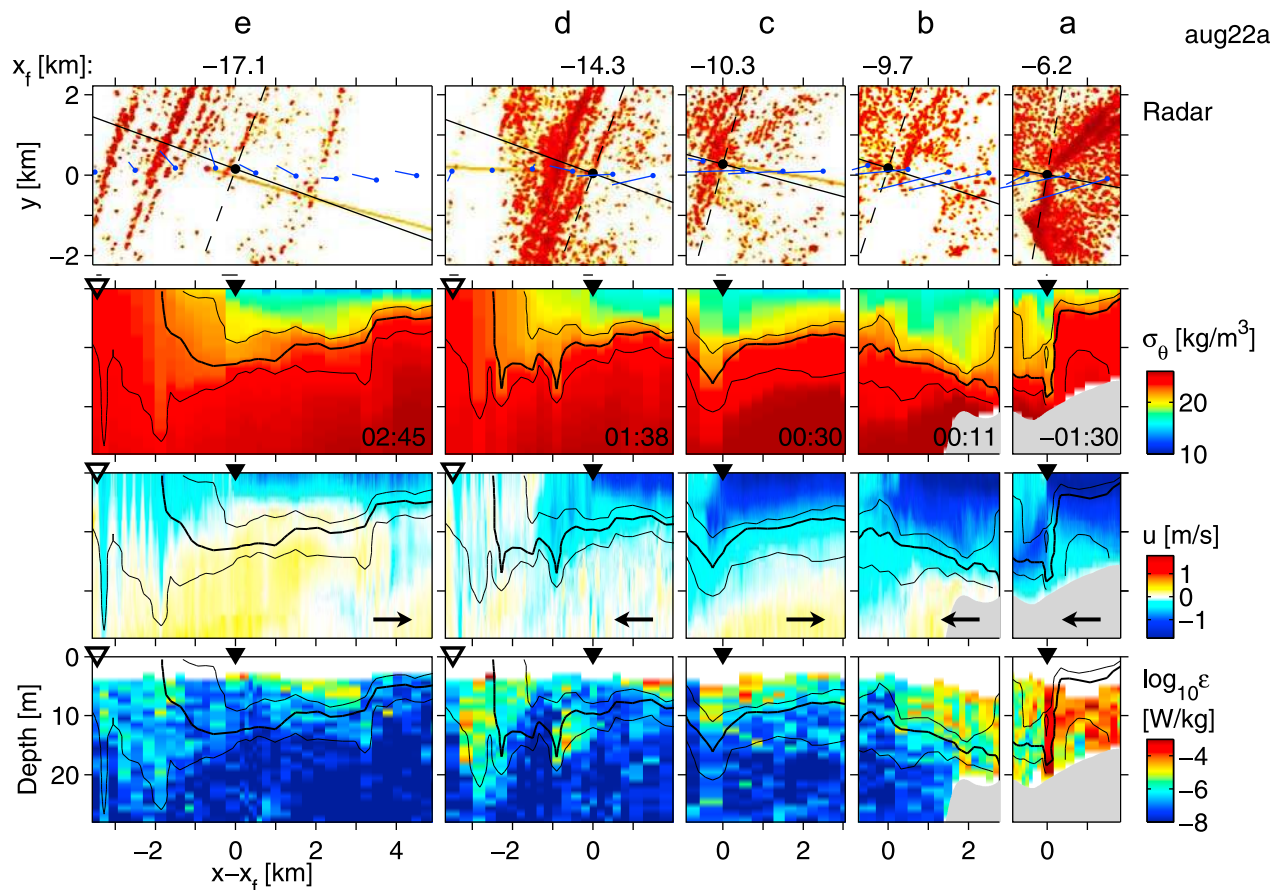
Figure 6. Transects across front aug22a. Blue surface velocity arrows are plotted over the radar images (1 km = 1 m/s). An open triangle marks the location of the lead wave in a NLIW train. All other plots and notations are as in Figure 5.

density decreased in the direction of propagation) were relatively common over the bar region during the initial stages of plume emergence, and were observed during ebbs aug21a, aug21b, aug22a and aug22b.

[49] As the reverse front moved offshore, it detached from the bottom and was supplied with increasingly buoyant fluid from the estuary, thus reducing its density. Eventually, densities onshore and offshore of the front became similar so that the cross-front surface density gradient was essentially nonexistent (Figure 6b). However, a subsurface velocity maximum still persisted ahead of the front (Figures 6b and 6c). In Figure 6c, this feature is associated with downward displacement of isopycnals and elevated turbulence ($\varepsilon = O(10^{-5}$ W/kg)).

[50] As the front moved into denser, less stratified water (Figures 6c and 6d) it became a "proper" front, with surface density increasing in the direction of propagation (offshore). In Figure 6d, multiple zones of surface density change and convergence exist. Two such features are identified: (1) the original "primary front" (filled triangle) and (2) a disturbance further offshore (open triangle). The latter is the lead wave in a train of NLIWs, identified primarily using velocity (Figure 6d, u) and acoustic backscatter. Based on their location and speed, they could have been generated near the bar as ebb began (having propagated ahead of the primary front on the elevated ambient stratification). How-

ever, they were not observed earlier, possibly due to the complexity near the bar.

[51] A band of elevated radar intensity (Figure 6d, radar) coincides with a zone of elevated surface convergence (Figure 6d, u) 1 km offshore of the primary front (inshore of the internal wave train). Between this feature and the primary front is a region of complex, wave filled, internal structure and intermediate density fluid.

[52] At first glance this appears to be a second front. In Figure 6e, however, the primary front has overtaken the intermediate density fluid (causing its density gradient to sharpen). The waves, on the other hand, have continued to propagate offshore ahead of the primary front, as indicated by parallel bands of elevated radar backscatter, $O(5–10$ m) isopycnal displacements, wave shaped pulses of offshore flow and elevated ε. Back in the plume, the rapid change in thickness 3.5 km inshore of the front (Figure 6e) is reminiscent of Garvine's trailing front (see his Figure 4).

[53] Tidal plume aug25b provides an alternate example of a complex front (Figure 7). This ebb was rather weak and occurred during a period of sustained upwelling winds (Figure 2). In this example a train of short-wavelength boluses formed ahead of the primary front (the lead disturbance is marked by an open triangle), visible in the acoustics but unresolved in the in situ profiles.

[54] As this front moved offshore, the sequence of boluses transformed into NLIWs with both larger amplitude and
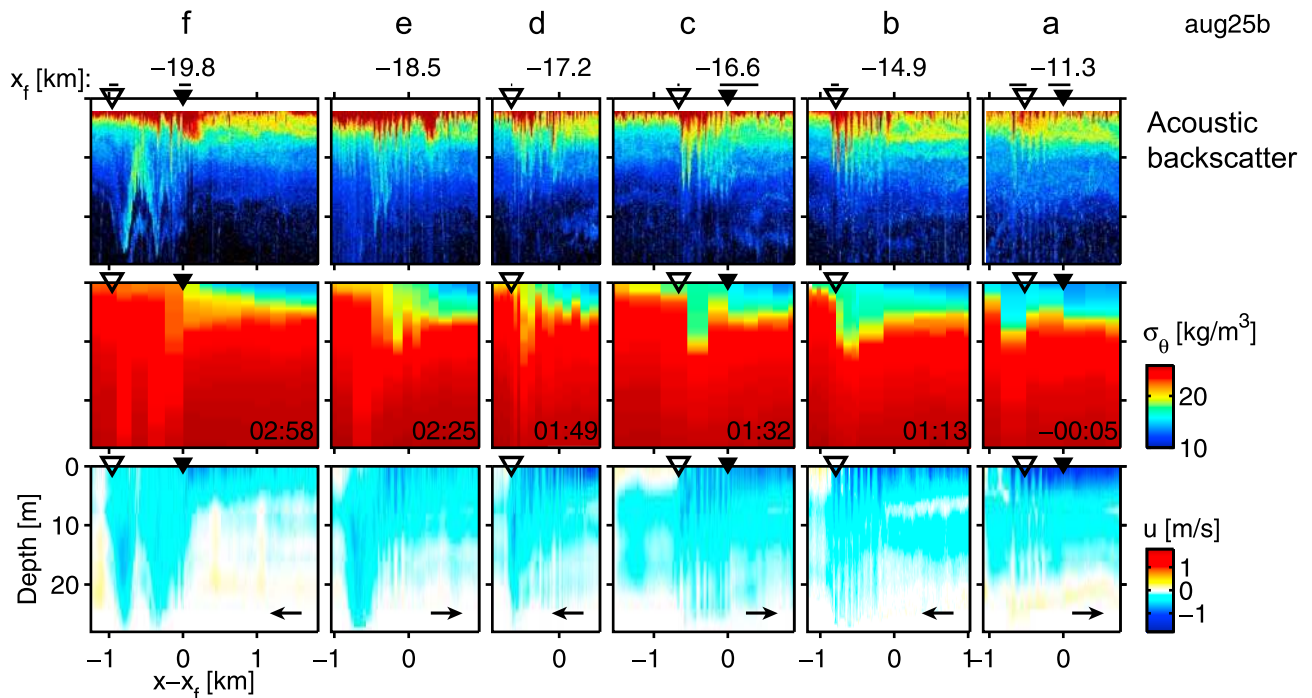
Figure 7. Transects across front aug25b. Log of acoustic backscatter from the 120 kHz Biosonics™ echo sounder. Front position ambiguity is indicated above. Density contours have been excluded. Potential density (σ_θ). Eastward velocity (u). All other notations are as in Figure 6.

wavelength. It is unclear whether individual boluses grew to become waves or whether the entire packet transformed. Regardless of this distinction, in the final transect (Figure 7f) two large NLIWs are apparent and the high-wave-number boluses are missing.

4. The Front as a Gravity Current

[55] In section 3 a considerable amount of variability in plume internal structure was described, especially near the river mouth. Part of the complexity is associated with strong bottom interactions that occur in the liftoff region that prevent the plume from expanding as a freely propagating gravity current. In the same region, reverse fronts (saltier water inshore of the front than offshore) were often observed. Ultimately, low-salinity fluid supplied to the front establishes a buoyancy anomaly conducive to an offshore-propagating surface gravity current. In the following, we focus on the region offshore of liftoff ($x < b \equiv -8$ km), where two classes of freely propagating fronts were observed: simple and complex.

[56] Simple fronts have internal structure of a classical gravity current [e.g., *Benjamin*, 1968; *Simpson*, 1982]. That is, (1) their is only one front, (2) horizontal velocity and density gradients across it are sharp and coincident, (3) shear and stratification are concentrated in the plume base, and (4) it often has a single head wave which displaces ambient fluid as much as 3 times the plume thickness. Such fronts occur when estuary fluid is released into quasi-uniform coastal waters.

[57] In complex fronts, maxima in horizontal density gradient and surface velocity convergence were not colocated. Complex fronts were observed when the near-surface ambient stratification was elevated, allowing disturbances to

propagate ahead of the primary front at speeds similar to frontal propagation. This is consistent with the modeling studies of *Stashchuk and Vlasenko* [2009], who showed that NLIW packets are more likely to form during periods of high near-surface ambient stratification.

[58] Elevated stratification sets up conditions for both reverse and complex fronts. The presence of this fluid is related to surface winds. During ebbs aug21a and aug21b winds were weak and it is possible that remnant fluid was retained in this region by a "bulge" circulation [*Yankovsky and Chapman*, 1997; *Horner-Devine*, 2009]. Alternatively, during ebbs aug22a and aug22b winds had reversed to upwelling and it seems possible that remnant fluid that had moved north in a coastal current was pushed south toward the estuary mouth where it interfered with these plumes.

[59] Regardless of their differences, we observe that all fronts (both simple and complex) exhibit similar characteristics once they have detached from the bar region. In particular, they all freely propagate as buoyant gravity currents. In the following, we summarize the intraebb evolution of all fronts and investigate interebb differences to characterize the source of the variability.

4.1. Front Timing and NLIW Emergence

[60] The spatial evolution of each front is summarized in Figure 8a. Over the "bottom interaction" region ($x_f > b$) the fronts generated by lesser ebbs (aug21a and aug22a) propagated slowly, $U_f^* < 0.5$ m/s (Figure 8b). As a result, t_b (the time the front crossed b) was ≈2 h later than that of greater ebbs. Variability in t_b is not strongly correlated with $\Delta\eta_\circ$, but is instead correlated with the diurnal inequality (see section 4.5). Also note that these ebbs encountered strong
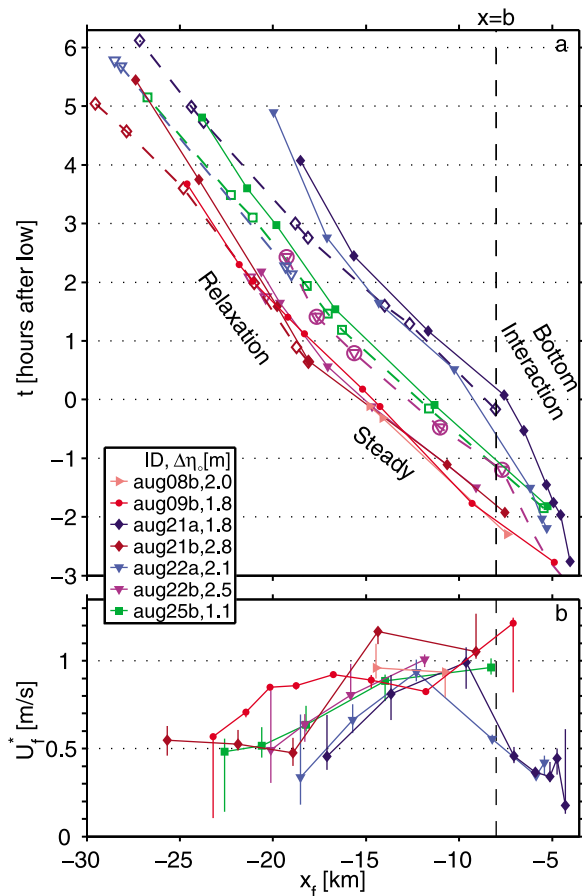
Figure 8. (a) Position x_f and (b) speed U_f^* (with error bars) for seven fronts. Solid lines and solid symbols indicate primary fronts; dashed lines and open symbols indicate the lead wave of the farthest offshore disturbance (NLIW) captured. One exception is the magenta dashed line with open circles and triangles that marks a secondary disturbance that trailed behind the primary aug22b front. A vertical dashed line at $b \equiv -8$ km marks the end of the shallow bar region (30 m isobath).

surface stratification over the bar region and resulted in complex fronts.

[61] Offshore of the bar (-15 km $< x < b$, labeled "steady") the trajectories of primary fronts (solid lines in Figure 8a) exhibited similar character, producing relatively constant U_f^* between 0.8 and 1.2 m/s (Figure 8b). At some point between $x = -15$ and -20 km (relaxation), front speeds decreased approximately linearly, except for aug21b, which encountered strong ambient currents (see section 4.3). The location of initial deceleration varied from ebb to ebb (Figure 8b), with weaker ebbs generally decelerating inshore of larger ones. Front deceleration continued until front speed was ≈0.5 m/s, after which time fronts were no longer a clearly identifiable feature in the measurements.

[62] Fronts aug21a, aug21b, aug22a, aug22b and aug25b each generated NLIWs that propagated through stratified ambient waters ahead of the primary front (Figure 8). Of these, only two NLIW packets (aug21b and aug22b) were clearly identified as having emerged from the deceleration of the primary plume front to below the NLIW wave speed

(the generation mechanism previously observed by *Nash and Moum* [2005] and modeled by *White and Helfrich* [2008]). Coincidentally, these were formed during the largest ebb pulses we sampled ($\Delta\eta_\circ = 2.8$ and 2.5 m).

[63] In contrast, during the lesser ebbs on these same 2 days, wave packets were not linked to rapid frontal decel-
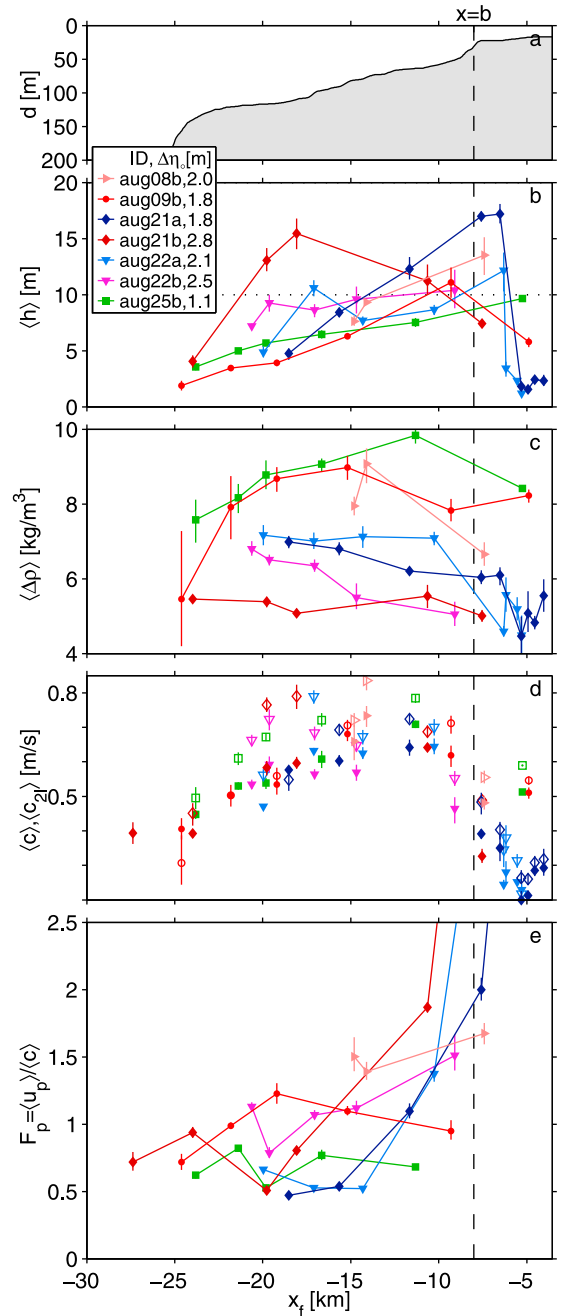
Figure 9. Spatial structure of plume properties behind the primary front. (a) Water depth, (b) plume thickness h, (c) density anomaly $\Delta\rho$, and (d) two-layer c_{2l} (open symbols) and first-mode wave speed c (solid symbols). (e) Plume Froude number F_p based on the local fluid velocity. Here $\langle \ \rangle$ denotes an ensemble average of profiles 0.5–3 km inshore of the front and are plotted versus the corresponding front location x_f. Error bars represent 95% bootstraps of each ensemble mean.

eration. For example, the lead NLIW generated during ebb aug21a was first observed ahead of the primary front at $x \approx b$, a time when it had been propagating relatively slowly. Similarly, NLIWs during aug22a were first identified more than 3 km from the primary front (Figure 6d). It is possible that both of these packets were generated from shocks ahead of reverse fronts in the bar region; however, details of this process were not resolved by our sampling. Waves generated during aug25b appeared during the breakdown of short-wavelength boluses. A common theme in the above examples is that wave radiation is connected with frontal propagation through remnant plume waters. Moreover, these observations also suggest the mechanism documented by *Nash and Moum* [2005] is not the exclusive means of NLIW generation in the Columbia River tidal plume system. The simple front of aug09b decelerated without radiating NLIWs, apparently due to the fact that it propagated into more weakly stratified ambient fluid that, unlike the above examples, presumably could not support NLIW radiation [*Stashchuk and Vlasenko*, 2009].

[64] In addition to waves excited ahead of the primary front, wave-like disturbances were also observed within the tidal plume itself. A secondary front during aug22b followed a similar trajectory to but 2 km inshore of the primary front (Figure 8a). Secondary fronts have been documented in many previous studies of spreading flows [e.g., *Scarpace and Green*, 1973; *McClimans*, 1978; LI87]. LI87 hypothesized that multiple fronts were caused by perturbations of the estuary discharge inshore of the initial front. These perturbations then formed frontal features of their own that propagated offshore on the coattails of the ebb. Alternatively, *Garvine* [1984] suggested that multiple fronts can arise even within quasi-steady forcing since the system is nonlinear and susceptible to shear instability. Both lab [e.g., *Rottman and Simpson*, 1984] and numerical [e.g., *Ungarish and Huppert*, 2004] studies confirm that spreading plumes often become undulating and produce multiple fronts.

4.2. Plume Thickness and Density

[65] The evolution and variability of the plume's dynamically important properties are shown in Figure 9. Plume thickness, h, is defined as the depth of the 30 salinity contour. Plume density, ρ_p, is then estimated as the mean density over $0 > z > -h$. With this, plume density anomaly

$$\Delta\rho = \rho_\circ - \rho_p \qquad (7)$$

can be computed ($\rho_\circ = 1026.3$ kg/m^3). Two-layer wave speed is computed as

$$c_{21} = \sqrt{g' \frac{h(d-h)}{d}}, \qquad (8)$$

where d is the water depth and $g' = \rho_\circ^{-1} g \Delta\rho$ is the reduced gravity. The first-mode long-wave speed within the plume, c, is computed numerically from N^2 profiles (no shear) [*Drazin and Reid*, 2004].

[66] While somewhat arbitrary, our definition of h is used for the purpose of estimating the vertical scale of tidal plume fluid, and not for dynamical calculations. Nevertheless, there is general agreement between c and c_{21} (c_{21} is

systematically biased 10% high; see Figure 9d) supporting h as an appropriate measure of plume thickness. c is used throughout the remainder of this work for dynamical interpretations.

[67] As discussed in section 3.2, the flow interacts strongly with the bottom over the shallow bar region where $d < L_m/3$ (Figure 9a). Sudden increases in h (Figure 9b) inshore of b are caused by the sudden arrival of buoyant fluid from upstream. However, this only weakly influences c and c_{21} because these variables depend more strongly on d than h (Figure 9d). As the water depth increases offshore of this region ($x < b$) wave speeds increase (d) and the plume no longer interacts with the bottom ($h \ll d$).

[68] Offshore of b, plumes aug09b, aug21a and aug25b thinned monotonically from $h \approx 10$ m (17 m for aug21a) at $x \approx -10$ km to $h \approx 5$ m by $x \approx -20$ km (Figure 9b). Plumes aug22a and aug22b deviate from this monotonic pattern by thickening briefly near $x \approx -17$ and -20 km, respectively. Plume aug21b was observed to thicken dramatically near $x = -18$ km, the details of which are explored in section 4.3.

[69] Intriguingly, $\Delta\rho$ tended to increase between $x = b$ and -20 km (Figure 9c). Since large x_f corresponds to later time, this result indicates that the ratio of advective buoyancy flux (supplied from upstream) to turbulent buoyancy flux (out of the plume, across its base) increases as time evolves. Considering that turbulent flux (integrated along the plume base) is unlikely to decrease as the plume expands and thins, the increase of $\Delta\rho$ offshore indicates that buoyancy supplied from upstream increases with time (consistent with *Nash et al.* [2009, Figure 8c]). This strongly contrasts the expected composition of a steady state river discharge, where entrainment must act to reduce plume $\Delta\rho$ with distance from the source, and highlights the importance of the time-dependent discharge strength and composition to plume evolution.

[70] While there is considerable ebb-to-ebb variability in both h and $\Delta\rho$ (Figures 9b and 9c), these combine to produce plumes with remarkably consistent patterns of wave speed, $c(x_f)$. Thicker plumes were generally associated with reduced $\Delta\rho$, so that c remained constant. This is consistent with h and $\Delta\rho$ variability being dominated by mixing, and is further supported by the fact that the thickest plumes occurred during spring tides, consistent with enhanced upstream mixing during these periods [*Nash et al.*, 2009].

[71] The plume Froude number ($F_p = u_p/c$, where u_p is the mean velocity within plume fluid behind the front ($0 > z > -h$); Figure 9e) is a measure of flow criticality within the plume waters. Near $x = b$, F_p is highly supercritical, due to a combination of strong plume velocities and weak c during the initial phase of the ebb. This suggests that information (i.e., from the plume front) is unable to propagate up estuary past the bar. Further offshore, the flow is approximately critical ($F_p = 1$).

[72] To summarize, the temporal increases in density combine with reduced h to produce a region of frontal propagation with remarkably constant c (5–10 km offshore of the bar). Only offshore of ≈ -15 km do h and $\Delta\rho$ decrease together, leading to reduced c and c_{21}. This reduction in c is attributed to plume thinning which we propose is linked to shutoff of the river discharge as ebb ends (section 5.3).
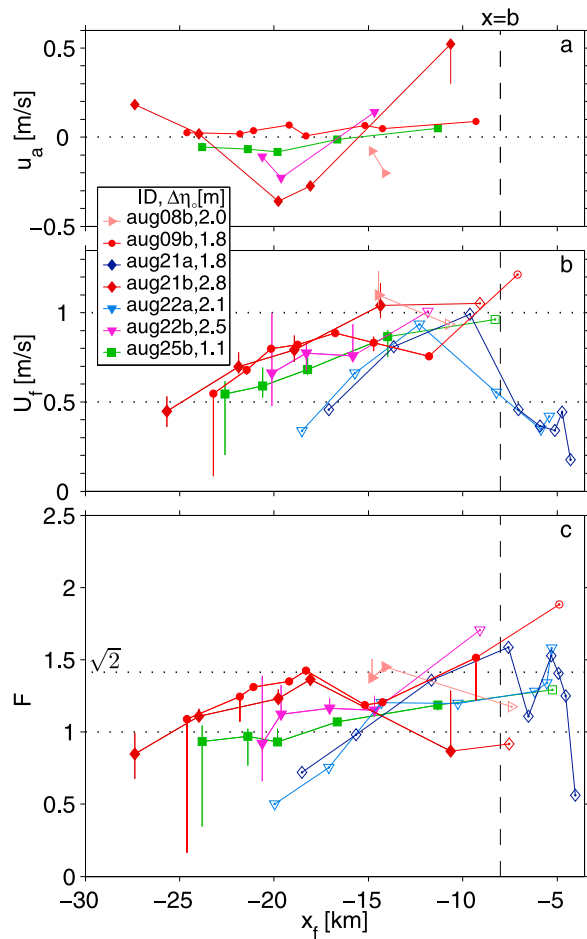
Figure 10. (a) Cross-front ambient velocity u_a (negative opposes front motion) and (b) primary front speed relative to the fluid ahead of it U_f with error bars. (c) Frontal Froude number. Open symbols are used for points in which we assume $u_a = 0$ and error bars could not be estimated.

4.3. Front Speed

[73] We define the front's propagation speed

$$U_f = U_f^* - u_a \tag{9}$$

relative to the motion of the ambient fluid u_a (Figure 10a) through which it propagates [*Benjamin*, 1968; *Simpson*, 1982]. Relative front speeds (Figure 10b) generally exhibit less interebb variability than U_f^* (Figure 8b). We compute u_a as the front-normal surface velocity 0.2 to 1.5 km offshore of the lead disturbance and averaged over the plume thickness ($0 > z > \langle -h \rangle$).

[74] Due to flow complexities, reliable estimates of u_a were not obtained over the bar ($x > b$), in some complex fronts (aug21a and aug22a), and when the ship did not transit offshore of the lead disturbance. In these cases, we assume $u_a = 0$ and plot U_f and F as open symbols (Figures 10b and 10c). We believe this to be reasonable considering that u_a was generally small compared with U_f^* (except during ebb aug21b). At $x \approx -11$ km, during ebb aug21b, because the flow structure ahead of the front was complex over a large region ahead of the front, this u_a estimate is likely to

be an overestimate of that quantity. In this instance we assign a subjective lower bound (0.3 m/s) that accounts for the notably high variability of the flow ahead of this front at this location.

[75] Offshore of b, all fronts begin with $0.8 < U_f < 1.1$ m/s. Fronts generated during greater ebbs maintain $U_f > 0.7$ m/s to $x \approx -20$ km before decelerating; during lesser ebbs (aug21a, aug22a) fronts decelerate farther inshore (at $x \approx -10$ to -15 km). Plots of U_f versus t (not shown) are roughly linear, indicating that once deceleration begins it is constant. This is not inconsistent with the result of *McCabe et al.* [2008], in which drifter velocities released during max ebb show initially large, followed by weaker, deceleration. Front and drifter speeds are very different quantities. Drifters were released inshore of the front and decelerated rapidly prior to reaching the front. After reaching the front, a major component of drifter speed was along front and therefore obscures front deceleration.

[76] One front strongly influenced by u_a was aug21b, which was the largest ebb sampled. It initially emerged in the presence of a strong offshore flow (near $x = -11$ km), then encountered a strong onshore flow near $x = -19$ km. Farther offshore the ambient velocity dropped to zero ($x = -24$ km) and reversed to offshore again ($x = -23$ km). Figure 10b shows that when this ambient velocity is accounted for, the evolution of ebb aug21b's front speed is similar to other fronts. This indicates that the earth frame deceleration of that front near $x = -18$ km (Figure 8b) is due to the strong onshore current (Figure 10a) that opposed the front's propagation. In the presence of this retarding u_a, and with the estuary discharge continuing to feed into it, the plume was forced to thicken (Figure 9b) through conservation of mass. Note also that front aug21b's $\Delta \rho$ was less than any other sampled, suggesting that enhanced mixing both within the plume and in the upstream estuary [*Nash et al.*, 2009] play some role in its thickness, since it was the strongest spring tide sampled. At $x \approx -24$ km the onshore flow stopped and the plume thinned abruptly to <5 m. The evolution of u_a (Figure 10a) and h (Figure 9b) suggest that front aug22b may undergo a similar, though weaker, process.

[77] Because we're concerned with rates of frontal propagation we define the frontal Froude number

$$F = \frac{U_f}{\langle c \rangle}, \tag{10}$$

with respect to the wave speed, c, within the plume [*Benjamin*, 1968]. This contrasts the definition used by *Nash and Moum* [2005] and *Stashchuk and Vlasenko* [2009] who showed that a Froude number based on wave speeds ahead of the front indicates whether internal waves were released from the front. Though poorly defined over the bar region (due to ambiguity in u_a and small c), F is initially (out to $x_f \approx -15$ km) in the range $1 < F < \sqrt{2}$. This range suggests that the front is propagating as an inertial gravity current [*Benjamin*, 1968; *Britter and Simpson*, 1978; *Marmorino and Trump*, 2000; *Shin et al.*, 2004] and therefore that plume c controls U_f. As the fronts move offshore and weaken, F drops below 1, suggesting that the fronts' motion is no longer driven by inertia-gravity balance [*Simpson*, 1982].
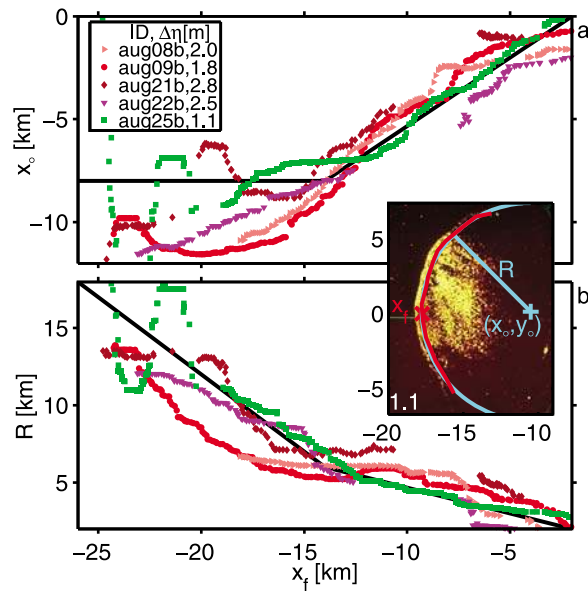
Figure 11. Front virtual origin $x_\circ$ and radius R versus plume front position x_f for five fronts. An inset radar image, 1.1 h after low tide aug09b, shows an example trace of front position (red line) and circle fit (cyan), all shifted to the right by 0.3 km. Here x_f, the point where the front crosses the x axis, is marked by a red cross. The fit variables, $(x_\circ, y_\circ)$, and R are labeled. The solid black line is a schematic representation of the data; see text for details.

[78] The ratio of F_p (Figure 9e) to F (Figure 10), which is equivalent to u_p/U_f, is larger near and over the bar than farther offshore ($x \approx b$), indicating that fluid supply to the front exceeds its propagation speed. This provides evidence for mixing and the rotor-like frontal circulation patterns described by LI87. Further from the bar this ratio approaches unity, possibly suggesting a decay in frontal turbulence further from the bar, consistent with the observed decrease in dissipation rate as the fronts decay (Figures 5 and 6).

4.4. Front Curvature and Virtual Origin

[79] Following LI87, we estimate the front's radius, R, and center (virtual origin), $(x_\circ, y_\circ)$, of curvature. These were computed using circle fits [*Gander et al.*, 1994] to traces of front position from the radar (Figure 11, inset). In order to reduce noise inherent in fitting a circle to an arc, a 1 h running median filter was applied to these estimates. Figure 11 shows $x_\circ$ and R, of five fronts as they propagated offshore. Fronts aug21a and aug22a have been excluded because the radar did not resolve the evolution of their curvature (see section 3.1). The virtual origin of most fronts was close to the x axis ($y_\circ \ll R$) and so we have not plotted $y_\circ$ here; aug25b is an exception with $y_\circ = O(-10$ km$)$.

[80] We identify two phases of front curvature evolution. During the initial "translation" phase, the virtual origin moved offshore from $x_\circ = 0$ to roughly -8 km at approximately 0.7 m/s, while R increased from 3 to 7 km at a rate of approximately 0.3 m/s. In the second "spreading" phase, the virtual origin is fixed near $x_\circ = -8$ km (-11 km for aug09b)

and $dR/dt \approx 0.5$–1.0 m/s is roughly equal to U_f^* (Figure 8) so that R increases one to one with x_f. These results are consistent with the model results of *Hetland and MacDonald* [2008], in which plume spreading was shown to increase with distance from the mouth of the Merrimack River.

[81] The spatial evolution of the Columbia River plume's expansion differs from the smaller-scale plume described by LI87. Specifically, LI87 showed that R and $x_\circ$ of the Koombana Bay plume both increased at similar, constant rates (each ≈ 0.11–0.16 m/s). In contrast, the Columbia is characterized by an early regime of rapid translation and weak spreading, followed by a period of more rapid radial expansion and slow to nonexistent translation of the plume's virtual origin.

[82] Some of these differences may be attributed to the influence of the Columbia River's shallow bar, which extends to 8 km, approximately the location of the plume's final spreading center. Over the bar, the outflow is constrained by the bottom (equation (6) and Figure 4), which prevents liftoff and hence free propagation as a gravity current. Instead, the transition to buoyant plume dynamics is delayed to the end of the bar ($x = b$), at which point approximately radial spreading occurs. Unlike LI87, the spreading center does not move offshore at this time because the bar becomes the transition point and source for the radially spreading plume.

4.5. Estuary Discharge

[83] In section 4.1, we suggested the extent and timing of spatial expansion (Figure 8) to be linked to variability in the tidal forcing $\eta(t)$. Following LI87 and *Chen* [1980], we anticipate these dynamics to be related to the time dependence of the estuary discharge, $Q(t)$. ADCP derived velocity from north-south transects across the river mouth at $x \approx -5$ km (lines 0 and 1 in Figure 1) were used to estimate estuary discharge

$$Q = - \iint u(y, z, t)\, \mathrm{d}y\, \mathrm{d}z \qquad (11)$$
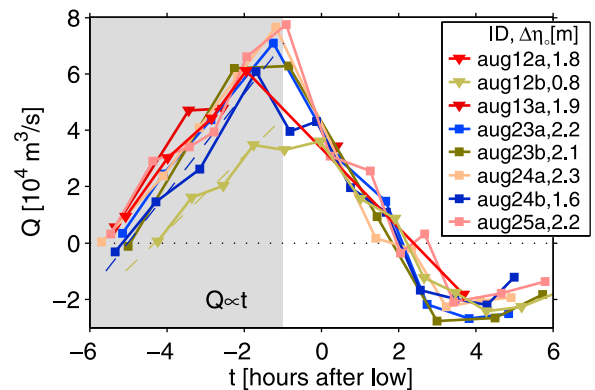
Figure 12. Tidal discharge Q as a function of t for eight ebbs (color). Triangles are from data collected along line 0, and squares are from data collected along line 1 (Figure 1). Dashed lines are example linear fits over the period of increasing ebb flow (shaded region) for ebbs aug12b and aug24b.
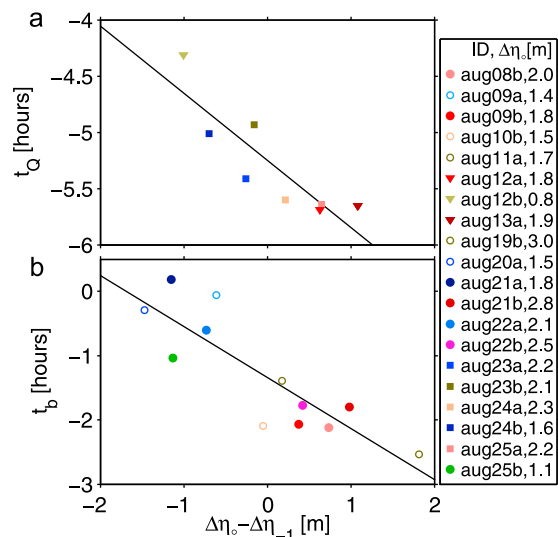
Figure 13. (a) Onset time t_Q of ebb flow at $x = -5$ km and (b) time of front crossing ($x_f = b$) versus diurnal inequality $\Delta\eta_\circ - \Delta\eta_{-1}$. Squares and triangles are computed from $Q(t)$ along lines 0 and 1, respectively (Figure 12). Solid circles represent t_b for the primary fronts in Figure 8; open circles represent fronts that were not tracked offshore but for which t_b could be estimated from radar images.

at each transect's mean time. Note that these transects occurred during different time periods than our front experiments (Figure 2), so we are unable to determine $Q(t)$ for the ebbs discussed so far. Instead, we use $Q(t)$ to understand the temporal evolution of the forcing, and how it varies with $\eta(t)$, which can be quantified for all time periods.

[84] During the period of increasing ebb flow ($-6 < t < -1$ h) Q increases linearly in time (Figure 12), similar to the result of LI87's discharge from Leschenault Estuary. $Q(t)$ peaks near $t = -1$ h, then sharply decreases as the ebb weakens; this evolution is nonsinusoidal. At $t = 2$ h $Q = 0$ after which the volume flux is into the estuary (negative Q) for the remainder of the tidal cycle.

[85] Straight line fits through the period of increasing ebb flow (Figure 12)

$$Q_{fit}(t) = \dot{q}(t - t_Q) \qquad (12)$$

were used to estimate the volume flux rate of change, $\dot{q}$, and onset time, t_Q, of offshore flow at $x \approx -5$ km. $\dot{q} = 4.8 \pm 0.3$ m^3/s^2 for all ebbs except aug12b during which $\dot{q} = 3.6$ m^3/s^2 (Figure 12).

[86] We initially believed that the time that the front crossed $x = b = -8$ km (t_b) and the time of ebb onset (t_Q) would be related to $\Delta\eta_\circ$, but we found these to be only weakly correlated. Instead, t_b and t_Q each show a much stronger correlation with the diurnal inequality (Figure 13). Both t_Q and t_b occur earlier for greater ebbs ($\Delta\eta_\circ > \Delta\eta_{-1}$). The similar magnitude of the dependence of these variables on $\Delta\eta_\circ - \Delta\eta_{-1}$ indicates that earlier ebbs, caused by larger tides, create fronts that emerge earlier. A good explanation why these vary more strongly with $\Delta\eta_\circ - \Delta\eta_{-1}$ than with $\Delta\eta_\circ$ is currently lacking. One possibility is that $\Delta\eta_\circ - \Delta\eta_{-1}$ is a measure of the salt content of the estuary (i.e., the salt

influx during the previous flood), and thus affects timing of plume emergence, but this has not been confirmed.

5. Plume Dynamics

[87] In section 4, we showed that Columbia River tidal plumes expanded with remarkable consistency, despite their complex internal structure. Here we highlight four aspects of the plume system which are important to our generalization of frontal evolution: (1) offshore of the bar ($x < -8$ km), plumes propagated with constant U_f for 5–10 km during a steady phase, after which U_f decreased slowly during a period of *relaxation*, (2) spatial patterns in U_f are tracked in c, leading to a constant frontal Froude number F, (3) plume front timing (relative to low tide) was related to the magnitude of the diurnal inequality $\Delta\eta_\circ - \Delta\eta_{-1}$, and (4) the tidal discharge near the river mouth $Q(t)$ exhibits a sawtooth evolution, in which it increases approximately linearly in time.

[88] In the following, we combine the above attributes to formulate a model for plume spreading offshore of the bar region. Specifically, we wish to explain why fronts initially propagate with relatively constant U_f. Front deceleration was weakest just after liftoff, then increases farther offshore. This contrasts the results of spreading plume models with steady $Q(t)$ in which front deceleration is highest near the mouth, and decreases offshore [*Garvine*, 1984; *Jay et al.*, 2010].

5.1. A Time-Dependent Spreading Model

[89] We follow LI87 and use *Chen*'s [1980] kinematic spreading plume model to include the time dependence of the source discharge in interpreting these observations. This contrasts the methodologies used by *Garvine* [1984] and *Jay et al.* [2010] which represent the plume dynamically but implicitly assume a time-invariant discharge. Our goal is to show the spatial dependence of U_f (Figure 8c) can be explained by Chen's simple kinematic model when fed by a time-variable discharge, $Q(t)$. For the purposes of this model we assume h can be considered spatially uniform inshore of the front (e.g., isopycnals are roughly horizontal in Figure 5b) and that, for a given ebb, $\Delta\rho$ is constant in time and space (Figure 9c).

[90] In making these assumptions we suggest that the time dependence of Q is more important to frontal evolution than mixing across the plume base. This is an alternate approach to several recent studies that suggest mixing is important to plume dynamics, particularly with respect to its influence on lateral spreading [*MacDonald et al.*, 2007; *Hetland and MacDonald*, 2008; *Hetland*, 2010]. We justify our approach in the following two ways: (1) Q exhibits O(1) variability (i.e., from 0 to max(Q)) and (2) we argue that this front propagates in gravity-inertia balance (opposed to gravity-viscous balance, which may be the case for smaller plumes [*Hoult*, 1972; *Chen*, 1980]). The latter point implies, to first order, that frontal propagation is controlled by plume internal wave speed [*Benjamin*, 1968], which is essentially unaffected by mixing (since $c^2 \propto h\Delta\rho$ remains constant as a layer thickens due to mixing). This assumption has both dynamic consequences, because $c \approx 0.7$ m/s is roughly constant over 10 km of frontal propagation (Figure 9d), and kinematic consequences, as the vertically integrated freshwater (and its transport) is also constant in space. Both of
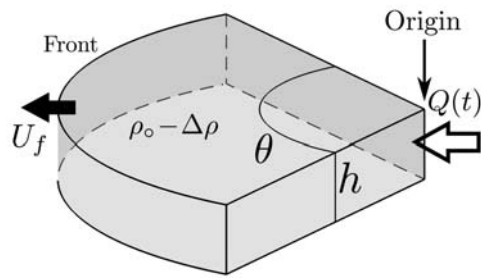
Figure 14. Perspective view of idealized geometry of *Chen*'s [1980] radially spreading plume model with time-dependent source volume flux $Q(t)$.

these attributes are preserved in our simplified plume geometry. Thus, while mixing is clearly important to the near-field plume composition [*Nash et al.*, 2009], we propose the basic plume geometry is set by the time-dependent characteristics of the source.

[91] This model begins with a kinematic representation of the plume, which spreads with density $\rho_\circ - \Delta\rho$ as a pie-shaped wedge into a semi-infinite ($d \to \infty$), motionless ambient of density $\rho_\circ$ (Figure 14). The thickness h, angle θ (in radians), and radius $R(t)$ give a plume volume

$$V(t) = \theta h R^2 / 2. \tag{13}$$

Direct estimates of θ were not made; for simplicity, we assume $\theta = 2$ (=115°). However, since variables that involve θ are estimates of scale, this choice does not alter interpretation. With the assumption of no entrainment, volume conservation is

$$Q(t) = \frac{dV}{dt}. \tag{14}$$

The front velocity is defined as

$$U_f = \frac{dR}{dt}. \tag{15}$$

[92] With $Q(t)$ and $\Delta\rho$ known, h and R are the undetermined variables of interest. As has been pointed out in many previous works [e.g., *Hoult*, 1972], volume conservation alone does not uniquely determine the plume depicted by Figure 14. An expression that relates U_f to h is required. Following previous gravity current studies [*Benjamin*, 1968; *Hoult*, 1972; *Chen*, 1980; *Didden and Maxworthy*, 1982; *Garvine*, 1984; *Shin et al.*, 2004] and in agreement with our own results (Figure 10c), we employ the frontal Froude number condition

$$F_{2l} = \frac{U_f}{c_{2l}} = \text{Constant}. \tag{16}$$

In this model, in which we assume $d \to \infty$ (no bottom interaction), (8) becomes $c_{2l} = \sqrt{g'h}$.

[93] Combining (13) with this frontal condition, employing (14), (15), and assuming that front acceleration is small ($dU_f/dt \ll U_f^2/R$), it is straightforward to show that

$$U_f = F_{2l}c_{2l} = \left(\frac{F_{2l}^2 Q'g'}{t}\right)^{1/4}. \tag{17}$$

Here $Q' = Q/\theta$ is the per radian volume source flux. U_f ($\propto c_{2l}$) and h are fully determined by $Q(t)$ according to (17), as originally derived by *Chen* [1980; also *Didden and Maxworthy*, 1982].

5.2. Two Limits of Model U_f

[94] Based on the observed time evolution of estuary discharge (Figure 12), we explore two limits of (17). In the first limit, we assume $Q'(t)$ increases linearly in time, $Q'(t) = \dot{q}'t$, where $\dot{q}'$ is a constant. This is consistent with the observed behavior of $Q(t)$ over the period of increasing ebb flow ($-5 < t < -1$ h). In this limit (which was also considered by LI87) the time dependence of (17) disappears so that

$$U_f = F_{2l}c_{2l} \approx (F_{2l}^2 g'\dot{q}')^{1/4}. \tag{18}$$

Thus, within the framework of this model, U_f = Constant is a consequence of linearly increasing $Q(t)$.

[95] During the second half of ebb, Q was found to abruptly decrease (Figure 12). As an approximation to this, we consider a second limit to (17) in which $Q = 0$, corresponding to the spreading of a fixed volume V of buoyant fluid. In this limit, we may rewrite (17) in terms of $V' = V/\theta$ to yield

$$U_f = F_{2l}c_{2l} \approx F_{2l}(V'g')^{1/2}R^{-1}. \tag{19}$$

Hence, $U_f \propto 1/R$ for a fixed volume of fluid ($Q = 0$).

[96] Based on the above limits, we expect $U_f \propto dQ/dt =$ Constant during the period of linearly increasing ebb flow. After Q ceases to increase, we expect U_f to decrease in space, scaling like $1/R$, with this decay set by $\int Q dt$. We use the observed $Q(t)$ to explore these limits in sections 5.3–5.5.

5.3. Plume Size and Front Timing

[97] The length scale L_{tidal} separating the two anticipated limits of (17) depends on the evolution of $Q(t)$ and its integral $V_{tidal} = \int_{ebb} Q dt$ over the period of positive ebb discharge, such that

$$L_{tidal} = \sqrt{\frac{2V_{tidal}}{\theta h}}. \tag{20}$$

Because the ebbs in Figure 12 are not the same as those that were front tracked, we parameterize V_{tidal} in terms of $\Delta\eta_\circ$. However, our sampling did not resolve a large dynamic range of $\Delta\eta_\circ$ so we use ROMS model output of the Columbia River estuary and near field to parameterize V_{tidal} in terms of $\Delta\eta_\circ$ [*MacCready et al.*, 2002]. A linear fit of model V_{tidal} (from model Q through line 0) to model $\Delta\eta_\circ$ (at 124.126W,46.24N) produces the empirical relationship

$$V_{tidal} = \left(3.2m^{-1}\Delta\eta_\circ + 1.9\right)10^8 m^3. \tag{21}$$

This relationship explains 91% of the variance in model V_{tidal} over a range of $\Delta\eta_\circ$ from 0.25 to 3.3 m. It also holds for estimates of V_{tidal} based on observed $Q(t)$ (Figure 12).

[98] In order to isolate the influence of V_{tidal} on L_{tidal} in (20), $h = 8$ m was used for all fronts. This methodology produced estimates of L_{tidal} that ranged from 8.2 km (aug25b) to 11.6 km (aug21b).
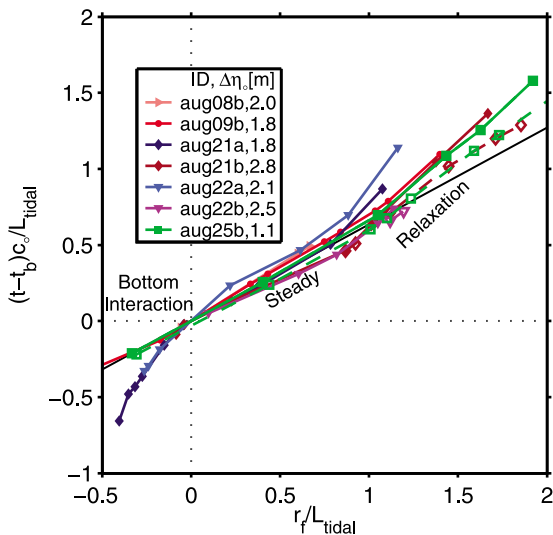
Figure 15. Nondimensional plume front timing of all fronts observed. Note that the offshore direction is now to the right (increasing r_f). Dashed lines and open symbols mark NLIWs radiated from the fronts near $r_f/L_{tidal} = 1$.

[99] Section 4.4 indicates that the spreading origin can be considered stationary near $x = b$. For convenience, we define front position offshore of this

$$r_f = b - x_f. \qquad (22)$$

Because x_f is the intersection of the front with $y = 0$, r_f may be considered a radial coordinate from the plume's presumed spreading center at $(x, y) = (b, 0)$. Throughout the remainder of this work $b = -8$ km except during ebb aug09b during which $b = -11$ km.

[100] When front timing is nondimensionalized as $[(t - t_b) \times c_\circ]/L_{tidal}$ and position as r_f/L_{tidal}, front timing versus position curves are similar for all fronts (Figure 15). Here, $c_\circ$ is the mean value of $\langle c \rangle$ in the range $-20 < x_f < -10$ km for each front. The slope of the best fit (black line) to the data between $0 < r_f < L_{tidal}$ is the Froude number, $U_f/c_\circ \approx \sqrt{2}$.

[101] Inshore of the bar ($r_f < 0$) several fronts propagated slowly (i.e., aug21a and aug22a), which we attribute to interaction with the bottom. Further offshore, linear and similar trajectories during the steady stage indicate that fronts are propagating with constant U_f and similar F. Frontal deceleration near $r_f/L_{tidal} = 1$ (where the plume volume reaches V_{tidal}) indicates the beginning of the relaxation stage. The fact that this deceleration occurs as the plume reaches its maximum volume indicates that the evolution of U_f is closely tied to $Q(t)$.

[102] As fronts aug21b, aug22b and aug25b decelerate near $r_f/L_{tidal} = 1$, they radiate NLIWs. This indicates that the deceleration which brings about NLIW radiation [*Nash and Moum*, 2005], occurs as the estuary discharge subsides and the plume volume approaches V_{tidal}. This suggests that the location of NLIW radiation may occur at the scale of the total estuary discharge, L_{tidal}, in other tidal plume systems as well. Note that internal waves were also generated near the bar region during aug21a, aug22a (not shown).

5.4. Steady Propagation

[103] During the steady stage of propagation ($r_f/L_{tidal} < 1$), U_f reaches a maximum value of 0.9 to 1.1 m/s and c is roughly constant at 0.7 ± 0.1 m/s (Figures 16a and 16b). Combining the observed value of $\dot{q}' = \dot{q}/\theta = 2.5$ m^3/s^2 (section 4.5) with $g' = 0.07$ m/s^2 and assuming $F_{2l} = \sqrt{2}$ gives $U_f \approx 0.8$ and $c_{2l} \approx 0.6$ (Figures 16a and 16b, $r_f < L_{tidal}$, black lines). Considering the highly idealized geometry
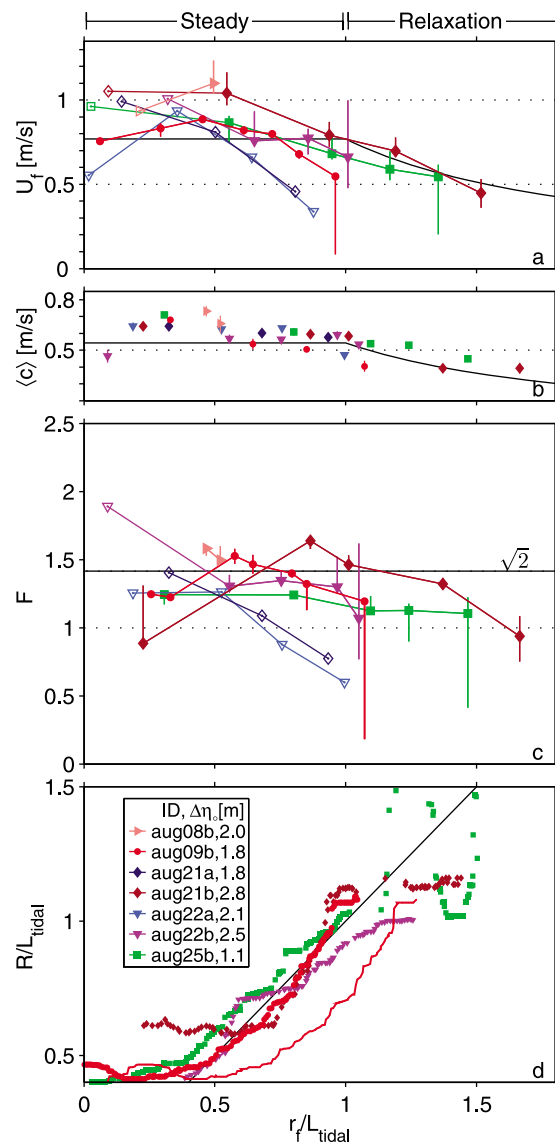
Figure 16. (a) Front speed, (b) plume first-mode wave speed, (c) frontal Froude number, and (d) R/L_{tidal} versus nondimensional position r_f/L_{tidal} for seven different fronts (color). Open symbols in Figures 16a and 16c indicate points for which we assume $u_a = 0$, and error bars could not be estimated. In Figure 16d, red dots mark aug09b with $b = -11$ km, and a thin red line is for aug09b with $b = -8$ km. All others, $b = -8$ km. Front aug08b has been excluded from Figure 16d because it was not resolved long enough to observe a period of expansion. Solid black lines indicate *Chen*'s [1980] solution.

(Figure 14), the level of approximation associated with (17) and the error in estimates of $\dot{q}$, the agreement of these values to observed initial speeds is reasonable. This suggests that the linear increase in $Q(t)$ forces the relatively constant (i.e., steady) U_f and c observed between $0 < r_f/L_{tidal} < 1$ (Figures 16a and 16b). Note also that fronts expand nearly radially through the latter half of the steady stage (Figure 16d). Agreement between front curvature data and the black $r_f = R$ line in Figure 16d indicates that these fronts are spreading from a roughly fixed virtual origin near $(x, y) = (b, 0)$. The better agreement of the red dots, compared to the thin red line, with the black line indicates that $b = -11$ km is appropriate for front aug09b.

5.5. Relaxation and Geostrophic Adjustment

[104] As ebb ends and the estuary discharge weakens, the relaxation stage ($r_f/L_{tidal} > 1$) begins. c decreases during this period as the plume continues to spread and thin. The evolution of U_f mirrors c, consistent with roughly constant F. This is consistent with (19), in which U_f and c decrease like R^{-1} as the fixed volume thins due to spreading (black curve, $r_f > L_{tidal}$, Figure 16).

[105] Eventually, offshore of $r_f/L_{tidal} = 1$, R approaches a limiting value of 1.1 to 1.5 L_{tidal}. At first glance this might suggest that L_{tidal} is not only the significant scale for plume front expansion, but also its final curvature. However, though Chen's [1980] theory predicts that the front will decelerate, it allows the plume to thin and expand indefinitely (Figure 16d, black line). With this in mind, we propose that the plume's expansion is limited by the Rossby radius

$$L_R = \frac{c}{f}, \tag{23}$$

where f is the Coriolis parameter. Taking $c \approx 0.7$ m/s gives $L_R \approx 7$ km. This value is remarkably similar to $L_{tidal} \approx 10$ km. This suggests that as the plume volume approaches V_{tidal} its dynamics are increasingly influenced by the Earth's rotation. As fluid parcels are deflected to the right surface convergence at the front will decrease. This being the case the plume front loses its buoyancy supply and will thin and decelerate. This suggests that the Coriolis effect is a second mechanism for frontal deceleration.

[106] The similarity between L_{tidal} and L_R is not a coincidence. Rewriting L_{tidal} in terms of the timescale of the estuary discharge, $\Delta t = (V_{tidal}/\dot{q})^{1/2}$, gives $L_{tidal} = Fc\Delta t$. Therefore the ratio of L_{tidal} to L_R is $F\Delta t/f$, which is independent of c. Instead, it is simply a ratio of the estuary (tidal) timescale, $\Delta t = O(6 \text{ h})$, to the inertial timescale, $1/f = O(4 \text{ h})$, which depends only on latitude. Thus, for mid- and high-latitude river plumes, we expect L_{tidal}/L_R to be $O(1)$.

[107] Ungarish and Huppert [1998] consider the effect of rotation on a finite volume lock release. The initial radius of the released fluid (stationary in the rotating frame) is $r_\circ$ and its initial Rossby radius is L_R. They find the radius of the "steady lens" solution to be

$$r_{SL} = r_\circ(1 + L_R/r_\circ). \tag{24}$$

Yankovsky and Chapman [1997] formulate a similar theory, but for a buoyant discharge with initial Froude num-

ber F rather than a lock release, and find the steady lens solution

$$r_{SL} = L_R \frac{3 + F_\circ^2}{\left(2 + F_\circ^2\right)^{1/2}}. \tag{25}$$

If we assume $L_{tidal} \approx 10$ km to be a good approximation of $r_\circ$, and $F_\circ \approx 2$ (Figure 9e, near $x = b$) then (24) and (25) give $r_{SL} \approx 17$ and 20 km, respectively.

[108] Agreement between these predictions of r_{SL} and the observed maximum radius of curvature, $R_{max} \approx 1.4 \ L_{tidal} \approx 14$ km, suggests that the final expansion of the plume is influenced by the earth's rotation. This being the case, this fluid has become a part of the bulge circulation [Horner-Devine, 2009] or one of the other far-field plume regimes [Yankovsky and Chapman, 1997; Hickey et al., 2005], depending on wind conditions.

[109] We therefore propose that the front's deceleration is driven by both the limited plume volume, V_{tidal}, and the effect of rotation. The former is likely to play a larger role as the front begins to decelerate and the latter apparently sets R_{max}. These results are consistent with the numerical model results of McCabe et al. [2009], in which the plume momentum balance is initially dominated by advective and pressure gradient terms, but eventually the Coriolis effect causes plume water to turn anticyclonically. While we expect these results are generally applicable to other tidal plume systems large enough to be considered inviscid, for systems with smaller river discharge it is possible that mixing will play a larger role in the tidal plume's dynamics [Hetland, 2010].

6. Conclusions

[110] The internal structure and three-dimensional expansion of tidal plume fronts that formed near the Columbia River mouth have been presented. Of seven fronts explored in detail, only two propagated as a single uncomplicated front (i.e., Figures 4 and 5), similar to that of a classical gravity current flowing through an unstratified or uniformly stratified fluid [i.e., LI87; Britter and Simpson, 1978; Garvine and Monk, 1974; Marmorino and Trump, 2000]. Instead, the majority of plumes had complex, non-classical internal structures that produced multiple fronts (Figures 6 and 7), similar to those observed by McClimans [1978], Garvine [1984], and LI87, or radiated nonlinear internal waves (NLIWs), as observed by Nash and Moum [2005]. Close to the river mouth, many fronts formed strong velocity convergences that did not coincide with horizontal density gradients. In many cases, the initial expansion was that of salty, dense fluid colliding with fresher, lighter receiving waters, producing what we term a reverse front. This complex behavior arises because (1) the estuary has strong temporal variability in both composition ($\rho(t)$) and flow rate $Q(t)$, (2) its discharge is constrained by shallow bathymetry, and (3) freshwater plume remnants are common in the vicinity of the river mouth. This work focuses primarily on the region offshore of the shallow bar ($x < -8$ km) where the plume evolves as a freely propagating gravity current.

[111] Even offshore of the bar, plume remnants from previous tidal cycles produce regions with strong horizontal

variability in stratification through which new plume waters propagate. This remnant fluid more readily supports NLIW radiation (i.e., as modeled by *Stashchuk and Vlasenko* [2009]) because internal wave speeds and plume front propagation speeds are more similar. Five of seven fronts supported NLIWs that propagated at a similar speed to, and offshore of, the primary front. One example exhibited a secondary front within the plume itself.

[112] Regardless of the internal complexity of the fronts, the intrinsic wave speed, c, and propagation speed, U_f, (relative to the ambient) had surprisingly similar spatial structure offshore of the bar, consistent from front to front (Figures 10b and 9d). Because these variables covary, their ratio, F, is roughly constant and in the range $1 < F < \sqrt{2}$ (Figure 10c), consistent with that expected for gravity current flows [*Shin et al.*, 2004; *Didden and Maxworthy*, 1982; *Marmorino et al.*, 2004] and observed by LI87. This provides strong additional support for the use of the constant F front condition (16) as a constraint to predict the relationship between U_f and c as the plume expands [i.e., LI87; *Chen*, 1980; *Garvine*, 1984].

[113] We have identified the following three periods of distinct dynamics that affect frontal evolution $U_f(t)$ (characterized in Figure 15): bottom interaction, steady, and relaxation phases.

[114] 1. As the plume emerges, it is initially strongly influenced by the shallow bar and is connected to the bottom over its first ≈ 8 km (i.e., $d < L_M/3$, equation (6)) [*Jones et al.*, 2007].

[115] 2. During the steady phase (i.e., just after liftoff) the front propagates freely as a gravity current with constant U_f. Timing of plume front emergence (liftoff) scales with the diurnal inequality.

[116] 3. As ebb weakens, the relaxation phase ensues and U_f decays. The location of deceleration is controlled by the total discharge volume V_{tidal} of each ebb, which sets the length scale L_{tidal} at which frontal deceleration occurs. L_{tidal} scales with the Rossby radius L_R, so that the tendency for the front to decelerate according to (19) is reinforced by a transition toward geostrophy.

[117] This classification of the Columbia River plume differs from that in Leschenault Estuary (LI87), which did not contain an extensive bottom-interacting region, nor did their analysis include the relaxation phase. However, in both cases, temporal variability of the estuary volume flux $Q(t)$ appears to control frontal expansion during the steady phase.

[118] Following LI87, we use the kinematic model of *Chen* [1980] to determine the evolution of U_f based on the time variability of Q. Conveniently, $Q(t)$ is observed to increase approximately linearly in time (in the Columbia and Leschenault estuaries). Chen's simplified geometry produces the result that $U_f =$ Constant during the linearly increasing discharge period, consistent with our observations. As ebb ends and $Q(t)$ begins to decrease, the plume evolution may be thought of as a spreading fixed volume (V_{tidal}) of buoyant fluid. This also represents a limit of Chen's model, yielding the solution that $U_f \propto 1/R$ in the relaxation phase, which begins at $R \sim L_{tidal}$.

[119] The similar magnitude of L_R and L_{tidal} suggests that as the plume volume approaches V_{tidal} the effect of the earth's rotation begins to play a significant role. Agreement of the plume's final radius of curvature, R_{max}, with simple spreading lens models encourages this idea. These results suggest that the Columbia River tidal plume front is initially driven by the linear increase in $Q(t)$, and as it expands beyond L_{tidal} it spreads like a fixed volume of fluid that becomes increasingly influenced by the earth's rotation.

[120] Our interpretation is fundamentally different from models of *Garvine* [1984] and *Jay et al.* [2010], which more accurately represent plume dynamics, but are limited to steady state applications. Those models typically predict initial front speed to decrease rapidly (strong deceleration) followed by weaker deceleration. In contrast, the model we employ assumes the time dependence of the source is more important for a radially spreading tidal plume than accurately representing the time variability of $\Delta\rho$ [*Jay et al.*, 2010] or the spatial variability of h [*Garvine*, 1984]. Following *Chen* [1980] and LI87, only the dynamics near the plume front are retained. However, the agreement with observed U_f validates these assumptions.

[121] In summary:

[122] 1. Offshore of the bar, the plume front expands at a constant U_f, which arises because of the time dependence of the estuary discharge flux. During this period, the plume flows as a gravity current with $1 < F < \sqrt{2}$.

[123] 2. The ultimate plume extent scales with L_{tidal}. Since L_{tidal} is proportional to L_R, this also represents the transition toward geostrophic balance, at which point the front becomes subcritical ($F < 1$);

[124] 3. Wind forcing alters the three dimensional plume shape and curvature of the plume front (Figure 3), but has only secondary effects on U_f.

[125] 4. Ambient currents alter propagation speed in the Earth's frame; the thickening of front aug21b as it flowed into an onshore current is an instructive example (section 4.3).

[126] This provides a synoptic understanding of tidal plume front evolution, from liftoff toward geostrophic adjustment, in terms of the time-dependent estuary discharge.

References

Alpers, W. (1985), Theory of radar imaging of internal waves, *Nature*, *314*, 245–247.

Benjamin, T. B. (1968), Gravity currents and related phenomena, *J. Fluid Mech.*, *31*, 209–248.

Bowden, K. F., and R. M. Gilligan (1971), Characteristic features of estuarine circulation as represented in the Mersey estuary, *Limnol. Oceanogr.*, *16*(3), 490–502.

Britter, R. E., and J. E. Simpson (1978), Experiments on the dynamics of a gravity current head, *J. Fluid Mech.*, *88*, 223–240.

Chen, J.-C. (1980), Studies on gravitational spreading currents, Ph.D. thesis, Calif. Inst. of Technol., Pasadena, Calif.

Didden, N., and T. Maxworthy (1982), The viscous spreading of plane and axisymmetric gravity currents, *J. Fluid Mech.*, *121*, 27–42.

Drazin, P. G., and W. H. Reid (2004), *Hydrodynamic Stability*, 2 ed., Cambridge Univ. Press, Cambridge, U. K.

Fong, D. A., and W. R. Geyer (2002), The alongshore transport of freshwater in a surface-trapped river plume, *J. Phys. Oceanogr.*, *32*, 957–972.

Fong, D. A., W. R. Geyer, and R. P. Signell (1997), The wind-forced response of a buoyant coastal current: Observations of the western Gulf of Maine plume, *J. Mar. Syst.*, *12*, 69–81.

Gander, W., G. H. Golub, and R. Strebel (1994), Least-squares fitting of circles and ellipses, *BIT Numer. Math.*, *34*, 558–578.

Garvine, R. W. (1974), Dynamics of small-scale oceanic fronts, *J. Phys. Oceanogr.*, *4*, 557–569.

Garvine, R. W. (1984), Radial spreading of buoyant, surface plumes in coastal waters, *J. Geophys. Res.*, *89*, 1989–1996.

Garvine, R. W., and J. D. Monk (1974), Frontal structure of a river plume, *J. Geophys. Res.*, *79*(15), 2251–2259.

Hansen, D. V., and M. Rattray Jr. (1966), New dimensions in estuary classification, *Limnol. Oceanogr.*, *11*, 319–326.

Hetland, R. D. (2010), The effects of mixing and spreading on density in near-field river plumes, *Dyn. Atmos. Oceans*, *49*(1), 37–53, doi:10.1016/j.dynatmoce.2008.11.003.

Hetland, R. D., and D. G. MacDonald (2008), Spreading in the near-field Merrimack River plume, *Ocean Modell.*, *21*, 12–21, doi:10.1016/j.ocemod.2007.11.001.

Hickey, B. M., G. N. Kachel, and A. MacFadyen (2005), A bi-directional river plume: The Columbia in summer, *Cont. Shelf Res.*, *25*, 1631–1656, doi:10.1016/j.csr.2005.04.010.

Hickey, B. M., et al. (2010), River influences on shelf ecosystems: Introduction and synthesis, *J. Geophys. Res.*, *115*, C00B17, doi:10.1029/2009JC005452.

Horner-Devine, A. (2009), The bulge circulation in the Columbia River plume, *Cont. Shelf Res.*, *29*, 234–251, doi:10.1016/j.csr.2007.12.012.

Horner-Devine, A., D. A. Jay, P. M. Orton, and E. Y. Spahn (2009), A conceptual model of the strongly tidal Columbia River plume, *J. Mar. Syst.*, doi:10.1016/j.jmarsys.2008.11.025.

Hoult, D. (1972), Oil spreading on the sea, *Ann. Rev. Fluid Mech.*, *4*, 341–368.

Jay, D. A., and J. D. Smith (1990), Residual circulation in shallow estuaries: 1. Highly stratified, narrow estuaries, *J. Geophys. Res.*, *95*, 711–731.

Jay, D. A., E. D. Zaron, and J. Pan (2010), Initial expansion of the Columbia River tidal plume: Theory and remote sensing observations, *J. Geophys. Res.*, *115*, C00B15, doi:10.1029/2008JC004996.

Jones, G. M., J. D. Nash, R. L. Doneker, and G. H. Jirka (2007), Buoyant surface discharges into water bodies. Part I: Flow classification and prediction methodology, *J. Hydraul. Eng.*, *133*, 1010–1020, doi:10.1061/(ASCE)0733-9429(2007)133:9(1010).

Luketina, D. A., and J. Imberger (1987), Characteristics of a surface buoyant jet, *J. Geophys. Res.*, *92*, 5435–5447.

MacCready, P., R. D. Hetland, and W. R. Geyer (2002), Long-term isohaline salt balance in an estuary, *Cont. Shelf Res.*, *22*, 1591–1601.

MacDonald, D. G., and W. R. Geyer (2004), Turbulent energy production and entrainment at a highly stratified estuarine front, *J. Geophys. Res.*, *109*, C05004, doi:10.1029/2003JC002094.

MacDonald, D. G., L. Goodman, and R. D. Hetland (2007), Turbulent dissipation in a near-field river plume: A comparison of control volume and microstructure observations with a numerical model, *J. Geophys. Res.*, *112*, C07026, doi:10.1029/2006JC004075.

Marmorino, G. O., and C. L. Trump (2000), Gravity current structure of the Chesapeake Bay outflow plume, *J. Geophys. Res.*, *105*(C12), 28,847–28,861.

Marmorino, G. O., A. L. Cooper, R. P. Mied, G. J. Lindemann, D. B. Trizna, and D. L. Porter (2004), Onshore propagation of a buoyant ocean front observed using a shore-based marine radar, *Cont. Shelf Res.*, *24*, 951–964.

McCabe, R. M., B. M. Hickey, and P. MacCready (2008), Observational estimates of entrainment and vertical salt flux in the interior of a spreading river plume, *J. Geophys. Res.*, *113*, C08027, doi:10.1029/2007JC004361.

McCabe, R. M., P. MacCready, and B. M. Hickey (2009), Ebb tide dynamics and spreading of a large river plume, *J. Phys. Oceanogr.*, *39*, 2839–2856, doi:10.1175/2009JPO4061.1.

McClimans, T. (1978), Fronts in fjords, *Geophys. Astrophys. Fluid Dyn.*, *11*, 23–34.

Moum, J. N., M. Gregg, R. C. Lien, and M. E. Carr (1995), Comparison of turbulence kinetic energy dissipation rate estimates from two ocean microstrucure profilers, *J. Atmos. Oceanic Technol.*, *12*(2), 346–366.

Moum, J. N., J. M. Klymak, J. D. Nash, A. Perlin, and W. D. Smyth (2007), Energy transport by nonlinear internal waves, *J. Phys. Oceanogr.*, *37*, 1968–1988, doi:10.1175/JPO3094.1.

Nash, J. D., and J. N. Moum (2005), River plumes as a source of large-amplitude internal waves in the coastal ocean, *Nature*, *437*, 400–403, doi:10.1038/nature03936.

Nash, J. D., L. F. Kilcher, and J. N. Moum (2009), Structure and composition of a strongly stratified, tidally pulsed river plume, *J. Geophys. Res.*, *114*, C00B12, doi:10.1029/2008JC005036. [Printed *115*(C2), 2010.]

Orton, P. M., and D. A. Jay (2005), Observations at the tidal plume front of a high-volume river outflow, *Geophys. Res. Lett.*, *32*, L11605, doi:10.1029/2005GL022372.

Rottman, J., and J. Simpson (1984), The initial development of gravity currents from fixed-volume releases of heavy fluids, in *Atmospheric Dispersion of Heavy Gases and Small Particles*, edited by G. Ooms and H. Tennekes, pp. 347–359, Springer, New York.

Scarpace, F., and T. Green III (1973), Dynamic surface temperature structure of thermal plumes, *Water Resour. Res.*, *9*, 138–153.

Shin, J. O., S. B. Dalziel, and P. F. Linden (2004), Gravity currents produced by lock exchange, *J. Fluid Mech.*, *521*, 1–34.

Simpson, J. E. (1982), Gravity currents in the laboratory, atmosphere, and ocean, *Ann. Rev. Fluid Mech.*, *14*, 213–234.

Simpson, J. E. (1997), Physical processes in the ROFI regime, *J. Mar. Syst.*, *12*, 3–15.

Spahn, E. Y., A. R. Horner-Devine, J. D. Nash, and L. F. Kilcher (2009), Particle re-suspension in the Columbia River plume near-field, *J. Geophys. Res.*, *114*, C00B14, doi:10.1029/2008JC004986. [Printed *115*(C2), 2010.]

Stashchuk, N., and V. Vlasenko (2009), Generation of internal waves by a supercritical stratified plume, *J. Geophys. Res.*, *114*, C01004, doi:10.1029/2008JC004851.

Ungarish, M., and H. E. Huppert (1998), The effects of rotation on axisymmetric gravity currents, *J. Fluid Mech.*, *362*, 17–51.

Ungarish, M., and H. E. Huppert (2004), On gravity currents propagating at the base of a stratified ambient: Effects of geometrical constraints and rotation, *J. Fluid Mech.*, *521*, 69–104, doi:10.1017/S0022112004000965.

White, B. L., and K. R. Helfrich (2008), Gravity currents and internal waves in a stratified fluid, *J. Fluid Mech.*, *616*, 327–356, doi:10.1017/S0022112008003984.

Yankovsky, A. E., and D. C. Chapman (1997), A simple theory for the fate of buoyant coastal discharges, *J. Phys. Oceanogr.*, *27*, 1386–1401.

L. F. Kilcher and J. D. Nash, College of Oceanic and Atmospheric Sciences, Oregon State University, 104 COAS Admin Bldg., Corvallis, OR 97331, USA. (lkilcher@coas.oregonstate.edu)